JM PAPERS

Linear response analysis of supersonic turbulent channel flows with a large parameter space

Xianliang Chen[1], Cheng Cheng[2], Lin Fu[1,2,3],† and Jianping Gan[1]

[1]Department of Mathematics and Center for Ocean Research in Hong Kong and Macau, The Hong Kong University of Science and Technology, Clear Water Bay, Kowloon, Hong Kong, PR China

[2]Department of Mechanical and Aerospace Engineering, The Hong Kong University of Science and Technology, Clear Water Bay, Kowloon, Hong Kong, PR China

[3]HKUST Shenzhen-Hong Kong Collaborative Innovation Research Institute, Futian, Shenzhen, PR China

In this work, the linear responses of turbulent mean flow to both harmonic and stochastic forcing are investigated for supersonic channel flow. Well-established universal relations are utilized to obtain efficiently the mean profiles with a large parameter space, with the bulk Mach number up to 5 and the friction Reynolds number up to 10^4, so a systematic parameter study is feasible. The most amplified structure takes the form of streamwise velocity and temperature streaks forced optimally by the streamwise vortices. The outer peak of the pre-multiplied energy amplification corresponds to the large-scale motion, whose spanwise wavelength (λ_z^+) is very insensitive to compressibility effects. In contrast, the classic inner peak representing small-scale near-wall motions disappears for the stochastic response with increasing Mach number. Meanwhile, the small-scale motions become much less coherent. A decomposition of the forcing identifies different effects of the incompressible counterpart and the thermodynamic components. Wall-cooling effects, arising with high Mach number, increase the spacing of the most amplified near-wall streaks; the spacing becomes nearly invariant with Mach number if expressed in semi-local units. Meanwhile, the coherence of stochastic response with $\lambda_z^+ > 90$ is enhanced, but on the other hand, with $\lambda_z^+ < 90$ it is decreased. The geometrical self-similarity of the response in the mid-λ_z range is still roughly satisfied, insensitive to Mach number. Finally, theoretical analyses of the perturbation equations are presented to help with understanding the scaling of energy amplification.

Key words: compressible boundary layers, turbulent boundary layers, supersonic flow

† Email address for correspondence: linfu@ust.hk

1. Introduction

Understanding and modelling high-speed turbulent flows are of fundamental importance in aerodynamic applications (Spina, Smits & Robinson 1994). The turbulent boundary layer influences surface drag and heat transfer dramatically. Thereby, developing accurate prediction models has long been the pursuit for reliable vehicle design. Compared with the incompressible case, our knowledge of compressible turbulent flows is rather limited, for two main reasons. First, the compressible flow suffers from coupling effects of various factors, which, in addition to the Reynolds number, include the Mach number, surface heat transfer, shock waves and high-enthalpy effects (Coleman, Kim & Moser 1995; Duan & Martín 2011; Fu *et al.* 2021; Fu, Bose & Moin 2022). Second, the available experimental and numerical databases are rather limited because of the restricted facilities and computational resources.

With the advancement of modern supercomputers, direct numerical simulations (DNS) (see e.g. Moin & Mahesh 1998) are increasingly powerful for the research of compressible turbulent flows. For example, recent DNS data from Zhang, Duan & Choudhari (2018) and Huang, Duan & Choudhari (2022) cover a freestream Mach number Ma_∞ range of up to 14 for flat-plate boundary layers with adiabatic and cold walls. In addition, the maximum friction Reynolds number Re_τ reaches as high as 4000 for the boundary layer (Pirozzoli & Bernardini 2013, with $Ma_\infty = 2$) and 2000 for the channel flow (Yao & Hussain 2020, with a bulk Mach number $Ma_b = 1.5$). Utilizing these DNS data, the effects of Mach number, wall cooling, pressure gradient, high-enthalpy, and so on, on turbulent scalings and structures, can be isolated and studied. For example, Duan, Beekman & Martín (2011) found that many of the scaling relations, though derived based on the Morkovin hypothesis, remained valid for boundary-layer flows with Ma_∞ up to 12. In addition, recent work of Di Renzo, Fu & Urzay (2020), Di Renzo & Urzay (2021) and Passiatore *et al.* (2022) demonstrated the applicability of these scaling relations on high-enthalpy boundary layers with thermochemical non-equilibrium effects.

Despite much progress, the parameter ranges of compressible turbulent DNS databases are still quite limited, especially for channel flows. The highest Ma_b reported for a channel flow is approximately 4 (Trettel & Larsson 2016). The Re_τ of that case is near 1000, but the centreline friction Reynolds number in semi-local units, $Re_{\tau,c}^*$, is only approximately 200. As mentioned above, the highest $Re_{\tau,c}^*$ of a channel flow case is reported by Yao & Hussain (2020), while the Ma_b of that case is limited to 1.5. Any effort to extend current parameter ranges is extremely resource-demanding. For example, the grid number in the case of Yao & Hussain (2020) is over 8 billion. If Ma_b is increased to 3 at the same Re_τ, then the required grid number is evaluated to be dauntingly over 20 billion. The substantial computational cost prohibits a systematic parameter study of various influencing factors.

Compared to instantaneous DNS data, the calculation of only turbulent mean flow can be substantially cheaper, such as through the Reynolds-averaged Navier–Stokes (RANS) or large-eddy simulations (LES) approaches. With only mean profiles in hand, one can still investigate some important turbulence characteristics using linear models, which will be introduced at length in § 1.2. Therefore, the combination of cheap reliable mean-flow calculation and the mean-flow-based analysis can be an effective way to explore the turbulence at high Mach and Reynolds numbers beyond the current capability of DNS. As a demonstration, Cossu, Pujals & Depardon (2009) and Hwang & Cossu (2010*b*) used a curve-fitted incompressible mean flow $Re_\tau > 10^4$, and analysed the transient growth and the responses to forcing for boundary-layer and channel flows. Pickering *et al.* (2021) proposed a resolvent-based model with the mean flow from LES and captured successfully the characteristics of turbulent coherent structures in the shear flow. This type of method

combination will be deployed in this work for canonical compressible channel flows. The focus is on the linear response of mean profiles and coherent structures, as an effort to extend the present knowledge frontier on the turbulence characteristics in high Mach and Reynolds number regimes beyond the scope of existing DNS databases. More specifically, the first aim is to utilize well-established universal relations to obtain turbulent mean profiles with a large parameter space. The second is to develop the linear response solvers to harmonic and stochastic forcing for compressible turbulent flows. The third is to investigate the response characteristics with varying Mach and Reynolds numbers, and provide supporting theoretical analysis.

1.1. *Universal relations for compressible wall-bounded turbulent flow*

It is well known that incompressible wall-bounded turbulent flows exhibit nearly universal mean streamwise velocity profiles versus the wall-normal coordinate when normalized with the wall viscous units. Therefore, a universal curve-fitted expression is available, and a prevailing one for the channel flow is from Cess (1958). This universal curve is also pursued in compressible turbulent flows for the mean velocity and temperature. For instance, the velocity transformation is designed to transform the compressible streamwise velocity profile to the incompressible counterpart. The pioneering work was accomplished by van Driest (1951), and subsequent improved versions were proposed by Zhang *et al.* (2012), Trettel & Larsson (2016), Volpiani *et al.* (2020), among others. Very recently, the total-stress-based transformation proposed by Griffin, Fu & Moin (2021*b*) collapses successfully nearly all available DNS data, with and without heat transfer, for the boundary-layer, channel and pipe flows. The relative errors are typically less than 3 % when $Re_\tau > 200$. Note that the performance of this transformation for non-canonical turbulent boundary-layer flows has been reported further in Bai, Griffin & Fu (2022). In terms of the temperature profile, Crocco (1932) and Busemann (1931) derived a temperature–velocity relation showing that the mean temperature was nearly a quadratic function of the mean streamwise velocity. Later, a less-restricted relation was proposed by Walz (1969) through introducing the recovery temperature. Furthermore, Duan & Martín (2011) made an improvement by introducing the mean enthalpy and provided more universal fitting coefficients for the quadratic expression based on the data of wide parameter ranges. This relation is shown to be sufficiently accurate for both boundary-layer and channel flows, even with high-enthalpy effects (Passiatore *et al.* 2022). Also, Zhang *et al.* (2014) proposed a general Reynolds analogy for compressible wall-bounded turbulent flows by introducing a general recovery factor.

The success of these universal relations makes it possible to obtain the mean profiles by solving an inverse problem under proper flow conditions in the outer region. This idea was adopted recently by Griffin, Fu & Moin (2022) to realize a highly accurate wall-modelled LES framework and to estimate the grid points required for DNS and LES (Griffin, Fu & Moin 2021*a*). For the channel flow with symmetric isothermal boundaries, Song *et al.* (2022) proposed an empirical relation between the centreline mean temperature and velocity. This can serve as an outer boundary condition to close the inverse problem, such that the mean-flow profiles can be obtained by solving a simple ordinary differential equation (ODE).

1.2. *Linear analysis of turbulent wall-bounded flows*

The linear models for analysing turbulent flows have received increasing interest, especially over the last decade (see McKeon 2017). This method of analysis shares some

fundamental procedures with linear stability theory, and borrows some critical thoughts from control theory (Taira *et al.* 2020; Jovanović 2021). The starting point is the linearized Navier–Stokes equation around a mean state for the Fourier-decomposed perturbation. The model equation can be written as

$$\mathcal{L}_{mn}\hat{q}_{mn} = \hat{f}_{mn}, \tag{1.1}$$

where $\mathcal{L}$ is a linear operator related to the mean flow as well as the temporal and spatial wavenumbers, the subscripts m and n are the Fourier indexes, and $\hat{q}$ denotes the perturbation shape function. The nonlinear term $\hat{f}$ was ignored in early works, and all the eigenmodes of $\mathcal{L}$ were found to be stable for the incompressible turbulent profile (Malkus 1956). Instead of discarding it totally, Reynolds & Hussain (1972) modelled the nonlinear term into the linear operator by using the Boussinesq approximation and the eddy viscosity μ_t. These eddy-viscosity-enhanced linear models have been adopted widely ever since. Better behaviour of artificially induced waves was reproduced in their results by considering μ_t, but the mean profile was still stable with $Re_\tau \sim 1000$.

As no unstable modes were found, linear model research was quiet for a while until two sets of mathematical tools were applied successfully. The first is the non-modal instability theory with pioneering work from Trefethen *et al.* (1993). Specifically, as the eigenvectors of $\mathcal{L}$ are not orthogonal to each other, $\hat{q}$ can experience strong transient growth even though each mode is asymptotically stable. This was identified by Butler & Farrell (1993) for incompressible channel flows. Furthermore, del Álamo & Jiménez (2006) (also Pujals *et al.* 2009) found that by using the eddy-viscosity-enhanced model, two peaks of the transient growth with different spanwise wavenumbers were well related to the near-wall motions and the outer-layer large-scale motions, respectively. The second methodology originates from control theory (Schmid & Henningson 2001; Kim & Bewley 2006; Zare, Georgiou & Jovanović 2020), and is called the input–output or resolvent analysis. By rewriting (1.1) as $\hat{q}_{mn} = \mathcal{L}_{mn}^{-1}\hat{f}_{mn}$ (this is an oversimplified interpretation and the theory details are presented in § 3), $\hat{f}$ is regarded as the input or forcing, and $\hat{q}_{mn}$ is the output or response. Their relation is established through the transfer matrix $\mathcal{L}_{mn}^{-1}$, known as the resolvent. Based on artificially selected forcing, the response characteristics of turbulent mean flow can be obtained through singular-value and Karhunen–Loève (KL) decompositions. Hwang & Cossu (2010*a,b*) analysed the linear responses to both harmonic and stochastic forcing for incompressible Couette and channel flows. Similar to the transient growth, the two most amplified structures are the near-wall and large-scale motions of infinite streamwise wavelength. As the most amplified modes can occupy a large portion of the response energy, they represent the characteristic flow structures, which can be deployed for reduced-order modelling. For example, through analysing the most amplified response, McKeon & Sharma (2010) emphasized the vital role of the critical layer for incompressible flows, where the phase velocity of the response equalled the mean velocity. The viscosity effects are significant in the critical layer, so their influence domain can extend well beyond the immediate vicinity of the wall. In the follow-up work, Moarref *et al.* (2013) designed a low-rank model based on the principal response mode. Different classes of scalings for the streamwise turbulence intensity were found.

The results of the above non-modal growth and resolvent analyses are also closely related. The strong resemblance was demonstrated among the amplified structures of transient growth, optimal harmonic and stochastic responses (Hwang & Cossu 2010*b*). Meanwhile, the linearly amplified modes all exhibit self-similarity in the mid-wavelength

range related to the logarithmic region (del Álamo & Jiménez 2006; Pujals *et al.* 2009; Moarref *et al.* 2013; McKeon 2019; Vadarevu *et al.* 2019), which provides mathematical evidence to the well-known attached-eddy model (AEM) initially proposed by Townsend (1976) (also see the recent review of Marusic & Monty 2019).

In most of the research mentioned above, the nonlinear forcing term $\hat{f}$ is modelled ideally, instead of an extraction from real flow data. Specifically, $\hat{f}$ is either assumed to be a stochastic signal or taken in an optimal form allowing for the strongest perturbation growth. Consequently, the results using the artificially designed forcing are more qualitative than quantitative, compared with the analysis based on DNS data (Zare, Jovanović & Georgiou 2017). The 'colour' of the forcing can lead to different weights of the amplified modes, potentially changing the relative importance of different modes. The weights of modes can be obtained by partly matching the DNS data. The resulting energy spectra and other statistics from the resolvent analysis are well consistent with those from DNS (Moarref *et al.* 2014; McMullen, Rosenberg & McKeon 2020). As another way of improvement, different optimization processes were designed by Zare *et al.* (2017) and Hwang & Eckhardt (2020) to obtain the cospectrum of the forcing signal, which is closer to realistic flows. To gain a complete understanding of the forcing statistics for incompressible turbulence, considerable efforts have been made recently to analyse the forcing based on the DNS data (Amaral *et al.* 2021; Morra *et al.* 2021; Nogueira *et al.* 2021). It is revealed that the forcing exhibits a relatively high level of spatial–temporal coherence. The low-rank nature of the forcing will benefit the construction of more reliable reduced-order models of turbulent flow. In addition, Morra *et al.* (2021) clarified why the introduction of μ_t in the linear operator leads to an improved response prediction compared to that without μ_t. That is because the weights or the combination coefficients of the principal resolvent modes are closer to those from DNS. In this sense, the usage of μ_t is also a partial modelling of the forcing colour, consistent with its low-rank nature.

The above results are mainly for incompressible turbulence. The extension and application of linear models to compressible turbulent flows are still limited. Alizard *et al.* (2015) first presented an analysis of linear transient growth on the turbulent boundary layers with Ma_∞ up to 4. The inner- and outer-layer modes, analogous to the incompressible ones, are identified, and the weak effects of compressibility are revealed on these characteristic structures. In addition to the similarities, an emerging problem is the dynamics of the suggested streaky temperature perturbation and its coupling with the velocity components. Recently, Bae, Dawson & McKeon (2020*a*,*b*) applied the resolvent formulation to supersonic turbulent boundary layers with both adiabatic and cold walls. Their results highlight distinct features below and above the relative sonic line of the response. Moreover, there are implications for the geometrically self-similar structure of response modes and the analogous rules for the incompressible counterpart. Dawson & McKeon (2020) investigated the same cases with emphasis on predicting the shapes of the resolvent mode at different Mach numbers. Up to now, to the authors' knowledge, the analysis framework of stochastic forcing and response has not been applied to supersonic turbulent flows, although there were successful attempts on the stability and receptivity of compressible laminar flows (Alizard *et al.* 2022; Madhusudanan & McKeon 2022), which demonstrates the feasibility and value of this linear framework in interpreting the physics of compressible flows. Therefore, a systematic study on the linear responses of supersonic turbulent flows to harmonic and stochastic forcing is required, which is the main focus of the present work.

1.3. *Streaky motions and compressibility effects*

Streamwise streaks are the most common coherent structures across different layers in wall-bounded turbulent flows. Their behaviours in incompressible flows have been studied in great detail, and are introduced briefly below (see e.g. Marusic *et al.* 2010*b*; Jiménez 2013, for more details). The streaks are narrow regions elongated in the streamwise direction, containing mainly the fluctuations of streamwise velocity. In the near-wall region, their mean streamwise length and spanwise spacing are approximately 1000 and 100 wall units in the buffer layer, first measured in experiments (Kline *et al.* 1967; Smith & Metzler 1983). Furthermore, they are dominant in carrying turbulence energy. The near-wall streaks are also known to be able to self-sustain along with the streamwise vortices, where the linear mechanisms of transient growth and instability play an essential role (Hamilton, Kim & Waleffe 1995; Schoppa & Hussain 2002). The streaky motions also exist at larger scales in the outer region, and are more often termed the large-scale or very-large-scale motions (Kim & Adrian 1999; del Álamo & Jiménez 2003). For the channel flow, the peak of the pre-multiplied spectra of streamwise velocity corresponds to characteristic streamwise and spanwise scales $5h$–$6h$ and h–$2h$, respectively (del Álamo & Jiménez 2003; Lee & Moser 2015), where h is the channel half-height. These large-scale motions are extremely energetic. Meanwhile, they are least affected by the presence of the wall; on the other hand, they have a modulation effect on the near-wall turbulence intensity (Hutchins & Marusic 2007; Marusic, Mathis & Hutchins 2010*a*).

In compressible flows, additional temperature and density streaks are present due to the wall-normal gradients of the mean flow (see e.g. Coleman *et al.* 1995). Superficial similarities of near-wall streaks were demonstrated in boundary-layer flows for the low, moderate and high Mach number (up to 12) cases (Duan *et al.* 2011). Meanwhile, two crucial features of compressibility effects on the near-wall motion are noted. The first is the variation of the spacing of streaks, on which different trends were reported. For example, wall cooling is shown to increase the streak spacing (Coleman *et al.* 1995; Duan, Beekman & Martin 2010), while the increase of *Ma* has a decreasing effect with an adiabatic wall condition (Duan *et al.* 2011). Further analysis shows that the spacing variation is consistent with the change of Re_τ^*. Therefore, the spacing experiences much less variation in semi-local units (Morinishi, Tamano & Nakabayashi 2004; Patel, Boersma & Pecnik 2016; Yao & Hussain 2020). The second feature is that wall cooling enhances the coherence of the near-wall motions. Meanwhile, the vortical structures become less chaotic (Coleman *et al.* 1995; Morinishi *et al.* 2004; Duan *et al.* 2010; Zhang *et al.* 2022). In comparison, the large-scale motions in the outer layer are less influenced by the compressibility effects from both experimental and numerical observations (Spina *et al.* 1994; Pirozzoli, Bernardini & Grasso 2008; Williams *et al.* 2018; Cheng & Fu 2022*a*).

The linear models of turbulence have long been used to investigate streaky motions. They are especially suitable for studying the structure, coherence and instability of streaks (see e.g. Schoppa & Hussain 2002; del Álamo & Jiménez 2006; Hwang & Cossu 2010*b*; McKeon & Sharma 2010). Nevertheless, as introduced in § 1.2, these linear models have rarely been deployed for compressible turbulent flows. The combination of the ODE mean-flow solver and the linear response analysis developed in this work enables a systematic study of the compressibility effects on the streaky motions in the channel flow. The parameter ranges considered are Ma_b from 0 to 5, and Re_τ up to 10^4, both of which are far beyond the current DNS database.

The remainder of the article is organized as follows. Section 2 describes the governing equations and the approaches to calculating the mean turbulent flow. Section 3 provides the formulation of the linear response analysis to both harmonic and stochastic forcing.
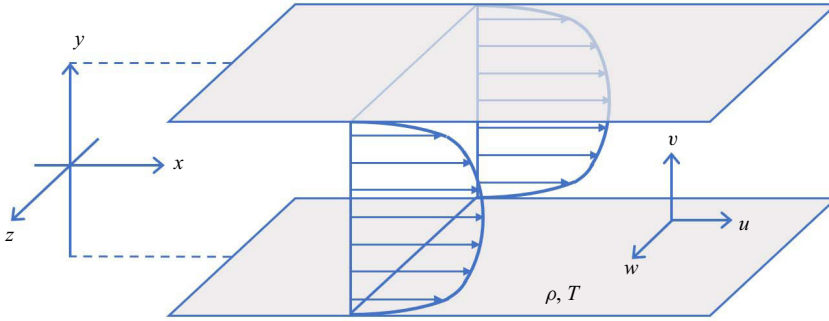
Figure 1. Schematic of the coordinate set-up for the channel flow.

The main results are discussed in § 4, and some theoretical proofs are provided in § 5. Finally, the work is summarized in § 6.

2. Governing equations and mean-flow calculations

2.1. *Compressible Navier–Stokes equations*

We consider a canonical compressible turbulent channel flow with symmetric isothermal boundaries. The flow illustration and coordinate set-up are shown in figure 1. With the assumption of a calorically perfect gas, the non-dimensional Navier–Stokes equations are written as

$$\frac{\partial \rho}{\partial t} + \nabla \cdot (\rho \boldsymbol{u}) = 0, \tag{2.1a}$$

$$\rho\left(\frac{\partial \boldsymbol{u}}{\partial t} + \boldsymbol{u}\cdot\nabla\boldsymbol{u}\right) = -\nabla p + \nabla\cdot\left[\frac{\mu}{Re_b}\left(\nabla\boldsymbol{u}+\nabla\boldsymbol{u}^{\mathrm{T}}\right)\right] - \frac{2}{3}\nabla\left(\frac{\mu}{Re_b}\nabla\cdot\boldsymbol{u}\right), \tag{2.1b}$$

$$\rho\left(\frac{\partial T}{\partial t} + \boldsymbol{u}\cdot\nabla T\right) - Ec\left(\frac{\partial p}{\partial t} + \boldsymbol{u}\cdot\nabla p\right) = \frac{Ec\,\mu}{Re_b}\left[\nabla\boldsymbol{u}:\left(\nabla\boldsymbol{u}+\nabla\boldsymbol{u}^{\mathrm{T}}\right) - \frac{2}{3}\left(\nabla\cdot\boldsymbol{u}\right)^2\right]$$
$$+\nabla\cdot\left(\frac{\kappa}{Re_b}\nabla T\right), \tag{2.1c}$$

$$p = \frac{\rho T}{\gamma Ma_b^2}, \tag{2.1d}$$

where ρ, $\boldsymbol{u} = [u, v, w]^{\mathrm{T}}$, p and T are the fluid density, velocity, pressure and temperature, respectively, and μ and κ are the viscosity and conductivity. For deriving (2.1), the following non-dimensionalizations are employed:

$$\left.\begin{array}{c} x = \dfrac{x^d}{h^d}, \quad \boldsymbol{u} = \dfrac{\boldsymbol{u}^d}{U_b^d}, \quad t = \dfrac{t^d U_b^d}{h^d}, \quad \rho = \dfrac{\rho^d}{\rho_b^d}, \quad p = \dfrac{p^d}{\rho_b^d U_b^{d2}}, \quad T = \dfrac{T^d}{T_w^d}, \\[2mm] \mu = \dfrac{\mu^d}{\mu_w^d}, \quad \kappa = \dfrac{\kappa^d}{\mu_w^d c_p^d}. \end{array}\right\} \tag{2.2}$$

The resulting Mach, Reynolds, Prandtl and Eckert numbers are defined as

$$Ma_b = \frac{U_b^d}{a_w^d}, \quad Re_b = \frac{\rho_b^d U_b^d h^d}{\mu_w^d}, \quad Pr = \frac{\mu^d c_p^d}{\kappa^d} = 0.72, \quad Ec = \frac{U_b^{d2}}{c_p^d T_w^d} = (\gamma - 1) Ma_b^2,$$

(2.3a–d)

where the superscript d stands for dimensional quantities, and the subscript w denotes quantities at the wall ($y = \pm 1$). Also, h is the channel half-height, and c_p is the isobaric specific heat. The speed of sound is $a^d = (\gamma R^d T^d)^{1/2}$, with R the gas constant, and the specific heat ratio $\gamma = 1.4$. The bulk density ρ_b^d and bulk velocity U_b^d are selected to meet the requirement

$$\int_{-1}^{1} \bar{\rho} \, dy = \int_{-1}^{1} \bar{\rho}\bar{u} \, dy = 2,$$

(2.4)

where the overbar denotes a mean variable. The viscosity is obtained through Sutherland's law, where the fitting constant is 110.4 K and the reference temperature is 293.15 K.

In wall-bounded turbulent flows, it is common to express the variables in wall viscous units with a superscript $+$ as

$$x^+ = \frac{x^d}{\delta_v^d}, \quad u^+ = \frac{u^d}{u_\tau^d}, \quad \rho^+ = \frac{\rho^d}{\rho_w^d}, \quad T^+ = \frac{T^d}{T_w^d} = T, \quad \mu^+ = \frac{\mu^d}{\mu_w^d} = \mu, \quad (2.5a\text{--}e)$$

where $u_\tau^d = \sqrt{\tau_w^d/\rho_w^d}$ is the friction velocity, τ_w is the wall shear, and $\delta_v^d = \mu_w^d/(\rho_w^d u_\tau^d)$ is the length unit. The corresponding friction Reynolds number is $Re_\tau = h^d/\delta_v^d$. Furthermore, Huang, Coleman & Bradshaw (1995) suggested a set of semi-local units for a better collapse of the turbulence statistics with the incompressible counterparts. The velocity and length units are based on the local mean density and viscosity as $u_\tau^{*d} = \sqrt{\tau_w^d/\bar{\rho}^d}$ and $\delta_v^{*d} = \bar{\mu}^d/(\bar{\rho}^d u_\tau^{*d})$, hence $y^* = y_d/\delta_v^{*d}$ and $Re_\tau^* = h^d/\delta_v^{*d}$. Hereinafter, the quantities using semi-local units are expressed with a superscript *.

The basic variable of (2.1) is $q = [\rho, u, v, w, T]^T$, which is decomposed into a mean part and a perturbed part as

$$q(x, y, z, t) = \bar{q}(y) + \tilde{q}(x, y, z, t),$$

(2.6)

where the mean component in the channel flow is taken as $\bar{q} = [\bar{\rho}(y), \bar{U}(y), 0, 0, \bar{T}(y)]^T$. The calculation of $\bar{q}$ is described in § 2.2, and the operations with $\tilde{q}$ will be elucidated in § 3.

2.2. *Calculation of turbulent mean flow*

For the incompressible channel flow, a semi-empirical expression proposed by Cess (1958) is used widely to describe the mean velocity profile $\bar{U}_{inc}^+$ at different Re_τ as

$$\left.\begin{aligned}
\bar{U}_{inc}^+(y^+; Re_\tau) &= \int_0^{y^+} \frac{1 - y^+/Re_\tau}{1 + \nu_t} \, dy^+, \\
\nu_t &= \frac{1}{2}\sqrt{1 + f_{\nu_t}^2} - \frac{1}{2}, \quad f_{\nu_t} = \frac{\kappa_c Re_\tau}{3}(1 - y^2)(1 + 2y^2)\left[1 - \exp\frac{Re_\tau(|y| - 1)}{A_{\nu_t}}\right],
\end{aligned}\right\}$$

(2.7)

where $\nu_t = \mu_t/\bar{\rho}$ is the kinematic eddy viscosity, and κ_c and A_{ν_t} are two fitting parameters. Based on the mean profile of $Re_\tau = 2003$, the values recommended by del Álamo &
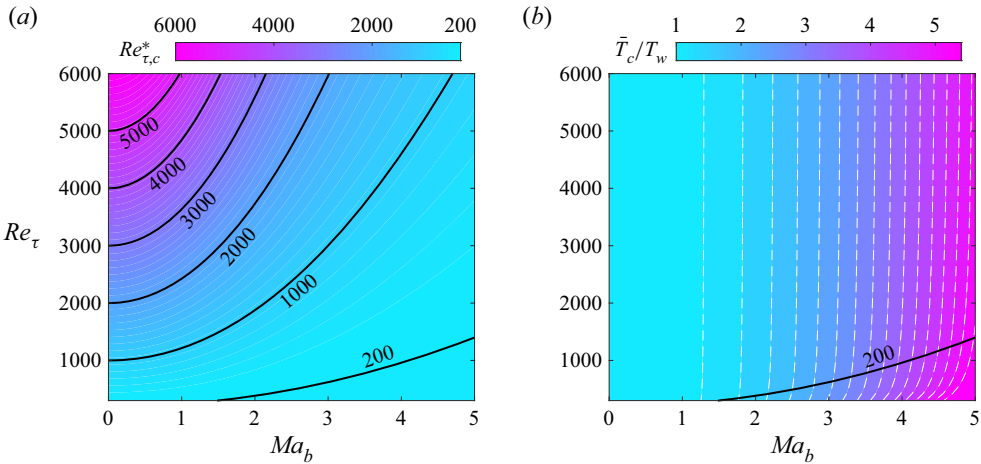
962 A7-8

Figure 2. Contours of (*a*) the friction Reynolds number in semi-local units $Re^*_{\tau,c}$, and (*b*) the centreline temperature. The black line in (*b*) is the contour line of $Re^*_{\tau,c} = 200$.

Jiménez (2006) are $\kappa_c = 0.426$ and $A_{\nu_t} = 25.4$, respectively. By including the DNS dataset of Re_τ up to 5200, the values adopted in the present work are $\kappa_c = 0.418$ and $A_{\nu_t} = 25.1$ for all Re_τ (see more details in Appendix A). The analytical equation (2.7) has been utilized widely in the linear and resolvent analyses of incompressible flows over wide parameter ranges (see e.g. Butler & Farrell 1993; del Álamo & Jiménez 2006; Moarref *et al.* 2013). However, no such expressions are currently available for the compressible channel flow.

As introduced in § 1.1, there are already adequate universal relations for solving the inverse problem. Consequently, the mean profile can be obtained quickly by solving an ODE. The algorithm involves four universal relations: (1) the incompressible velocity profile as shown in (2.7); (2) the compressible velocity transformation from Trettel & Larsson (2016) or Griffin *et al.* (2021*b*); (3) the algebraic relation from Duan & Martín (2011) between the temperature and velocity distributions; (4) the outer boundary condition from Song *et al.* (2022) connecting the centreline temperature and velocity. Only two parameters are required as the inputs, i.e. Ma_b and Re_τ (or equivalently, Re_b, Re^*_τ or others), and the solution takes less than one second on a laptop. The algorithm and the solver verification are elaborated in Appendix A.

With this efficient solver in hand, the mean turbulent flow of wide ranges of Re_τ and Ma_b can be obtained. As a demonstration, figure 2 depicts the contours of $Re^*_{\tau,c}$ and $\bar{T}_c$ as functions of Re_τ and Ma_b, with subscript c denoting the channel centre. The black contour with $Re^*_{\tau,c} = 200$ denotes the lower available boundary of the solver. As can be seen, at a fixed Re_τ, $Re^*_{\tau,c}$ drops rapidly with the increase of Ma_b, which heavily restricts the range of $Re^*_{\tau,c}$ of the DNS database. The present solver enables us to explore the flow characteristics far beyond the parameter range of the DNS database. Although its accuracy cannot be directly proved rigorously, the following three facts further strengthen our confidence in high Ma_b and Re_τ regimes.

(i) The velocity transformation (see (A2)) has been verified for flows with Ma_b up to 14, and tends to be more accurate at higher $Re^*_{\tau,c}$ (Trettel & Larsson 2016; Griffin *et al.* 2021*b*).

(ii) The accuracy of the velocity–temperature relation (see (A3)) has been proved for flows with Ma_b up to 14 (Duan & Martín 2011).

(iii) The $\bar{T}_c$ shown in figure 2(b) is insensitive to Re_τ when $Re_{\tau,c}^* > 200$. Meanwhile, $\bar{T}_c$ increases at a comparable speed with the adiabatic wall temperature (Song *et al.* 2022).

It is worth mentioning that the ratio of $\bar{T}_c/T_w$ increases quickly with Ma_b rise. For example, $\bar{T}_c/T_w$ is over 5.2 at $Ma_b = 5$. This results in a relatively large temperature gradient, and hence strong heat transfer at the wall. Therefore, the supersonic channel flow case can be considered as a highly cooled wall case in analogy to the boundary-layer flow. In this sense, the increase of Ma_b in the channel flow leads to a wall-cooling effect simultaneously, which will be discussed further in §4.3. It is also important to note that since $T_w < \bar{T}_c$, Re_τ^* decreases with Ma_b rise, as shown in figure 2(a), contrary to the trend of an adiabatic or moderately cooled wall boundary-layer case with $T_w > T_\infty$.

3. Formulation of the linear response analysis

3.1. *Linearized Navier–Stokes equation*

To study the characteristics of $\tilde{q}$, (2.1) is linearized around the mean state $\bar{q}$. The resulting equation of $\tilde{q}$ is written into a matrix form as

$$
\boldsymbol{F}\frac{\partial \tilde{q}}{\partial t} + \boldsymbol{A}\frac{\partial \tilde{q}}{\partial x} + \boldsymbol{B}\frac{\partial \tilde{q}}{\partial y} + \boldsymbol{C}\frac{\partial \tilde{q}}{\partial z} + \boldsymbol{D}\tilde{q}
$$
$$
= \boldsymbol{H}_{xx}\frac{\partial^2 \tilde{q}}{\partial x^2} + \boldsymbol{H}_{yy}\frac{\partial^2 \tilde{q}}{\partial y^2} + \boldsymbol{H}_{zz}\frac{\partial^2 \tilde{q}}{\partial z^2} + \boldsymbol{H}_{xy}\frac{\partial^2 \tilde{q}}{\partial x\,\partial y} + \boldsymbol{H}_{yz}\frac{\partial^2 \tilde{q}}{\partial y\,\partial z} + \boldsymbol{H}_{xz}\frac{\partial^2 \tilde{q}}{\partial x\,\partial z} + \tilde{N}, \quad (3.1)
$$

where the first eleven terms are linear terms of $\tilde{q}$, and $\tilde{N}$ collects all the nonlinear terms. The coefficients $\boldsymbol{F}$, $\boldsymbol{A}$, $\boldsymbol{B}$, $\boldsymbol{C}$, $\boldsymbol{D}$ and $\boldsymbol{H}$ are all 5×5 matrices related only to $\bar{q}$. Their specific expressions are listed in Appendix C.

In a turbulent flow, $\tilde{q}$ and $\tilde{N}$ can have large amplitudes. To facilitate the prediction capability of the linear model, turbulence models are used for the linearization of $\tilde{N}$, such as the widely used eddy-viscosity-enhanced linear model. The introduction of μ_t leads to better results in predicting the response growth, because it partially models the 'colour' of the nonlinear forcing term (Moarref & Jovanović 2012; Morra *et al.* 2019, 2021). In compressible flows, however, the expression of $\tilde{N}$ is far more complicated than its incompressible counterpart. Following Alizard *et al.* (2015) (also Pickering *et al.* 2021), two substitutions in (3.1) are made for the turbulence modelling, i.e.

$$
\bar{\mu} \to \bar{\mu} + \mu_t, \quad \bar{\kappa} \to \bar{\kappa} + \kappa_t = \frac{\bar{\mu}}{Pr} + \frac{\mu_t}{Pr_t}. \quad (3.2a,b)
$$

Here, κ_t and Pr_t are the turbulent heat conductivity and Prandtl number, and μ_t and κ_t are non-dimensionalized in the same way as μ and κ in (2.2). The assumptions behind (3.2a,b) are the Boussinesq assumption and the classic Reynolds analogy. The usage of the former is analogous to the incompressible counterpart. The deployment of the latter assumes implicitly that subject to the modelled part of the forcing, the diffusion of the internal energy of the response is proportional to the Reynolds stress part. We give more remarks on the usage of (3.2a,b). The two assumptions above may not be very accurate throughout the flow field. Nevertheless, the introduction of μ_t and κ_t can improve the prediction performance of the linear model as long as the modelling points to the 'right direction'. This is satisfied here for the canonical channel flow, which is away from the

962 A7-10

destruction of separation bubbles, shock/boundary-layer interactions, shedding vortex, etc. In this relatively 'clean' turbulence, the RANS models have proven their capability extensively (Wilcox 2006). Furthermore, as noted by Cossu *et al.* (2009) and will be shown in § 3.4, the results of the most amplified response are not very sensitive to the shapes of μ_t and Pr_t.

3.2. *Responses to harmonic and stochastic forcing*

As the mean flow is homogeneous in the streamwise and spanwise directions, the following Fourier decomposition is applied on $\tilde{q}$ as

$$\tilde{q}(x, y, z, t) = \iint_{-\infty}^{\infty} \hat{q}(y, t) \exp\left[i(k_x x + k_z z)\right] dk_x \, dk_z, \tag{3.3}$$

where k_x and k_z are the streamwise and spanwise wavenumbers, respectively, and $\hat{q}$ is the shape function. The same decomposition is performed on $\tilde{N}$. The resulting $\hat{N}$ involves the convolution of $\hat{q}$ components due to the nonlinearity.

After substituting (3.3) into (3.1), the following equation is arrived at for a single mode with $k_x \neq 0$ or $k_z \neq 0$:

$$\boldsymbol{F}\frac{\partial \hat{q}}{\partial t} + \hat{\boldsymbol{D}}\hat{q} + \hat{\boldsymbol{B}}\frac{\partial \hat{q}}{\partial y} + \hat{\boldsymbol{C}}\frac{\partial^2 \hat{q}}{\partial y^2} = \hat{N}, \tag{3.4}$$

where the rearranged matrices are

$$\left.\begin{aligned}
\hat{\boldsymbol{D}} &= \boldsymbol{D} + ik_x\boldsymbol{A} + ik_z\boldsymbol{C} + k_x^2\boldsymbol{H}_{xx} + k_xk_z\boldsymbol{H}_{xz} + k_z^2\boldsymbol{H}_{zz}, \\
\hat{\boldsymbol{B}} &= \boldsymbol{B} - ik_x\boldsymbol{H}_{xy} - ik_z\boldsymbol{H}_{yz}, \\
\hat{\boldsymbol{C}} &= -\boldsymbol{H}_{yy}.
\end{aligned}\right\} \tag{3.5}$$

Equation (3.4) can be rewritten into a standard form as

$$\frac{\partial \hat{q}}{\partial t} = L\hat{q} + \hat{f}, \quad L = -\boldsymbol{F}^{-1}\hat{\boldsymbol{D}} - \boldsymbol{F}^{-1}\hat{\boldsymbol{B}}\frac{\partial}{\partial y} - \boldsymbol{F}^{-1}\hat{\boldsymbol{C}}\frac{\partial^2}{\partial y^2}, \quad \hat{f} = \boldsymbol{F}^{-1}\hat{N}, \tag{3.6a--c}$$

where L is a linear operator, and $\hat{f} = [\hat{f}_\rho, \hat{f}_u, \hat{f}_v, \hat{f}_w, \hat{f}_T]^{\mathrm{T}}$ is the forcing term.

Before discussing the energy amplification of responses, an energy norm of $\hat{q}$ (E) needs to be defined. For compressible flows, a widely used form was proposed by Chu (1965) as

$$\|\hat{q}\|^2 = (\hat{q}, \hat{q})_E = \int_{-1}^{1}\left(\bar{\rho}\hat{u}^H\hat{u} + \frac{R\bar{T}}{\bar{\rho}}\hat{\rho}^{\dagger}\hat{\rho} + \frac{\bar{\rho}c_v}{Ec\,\bar{T}}\hat{T}^{\dagger}\hat{T}\right)dy = \int_{-1}^{1}\hat{q}^H\boldsymbol{M}\hat{q}\,dy \equiv 2\hat{E}, \tag{3.7}$$

under the current definition of non-dimensionalization. Here, the superscript † stands for the complex conjugate, $c_v = c_v^d/c_p^d = 1/\gamma$, $\boldsymbol{M}$ is a diagonal matrix, and $\hat{E}$ is the energy norm. Compared to the kinetic energy used in incompressible flows, (3.7) additionally considers the contribution from the acoustic and entropy components of $\hat{q}$ (see e.g. Chen, Wang & Fu 2022). More importantly, from the numerical point of view, $\boldsymbol{M}$ is strictly positive definite, which guarantees the invertibility of the transfer matrix (see (3.9*a,b*)).

For later use, we re-express (3.7) after the wall-normal discretization (see § 3.3 for details) in a vector form as

$$(\hat{q}, \hat{q})_E = \hat{Q}^H G_{MI} \hat{Q} \equiv \hat{Q}_{MI}^H \hat{Q}_{MI}, \quad \hat{Q}_{MI} = G_{MI}^{1/2} \hat{Q}, \qquad (3.8a,b)$$

which is convenient for applying standard matrix functions. Here, the global vector $\hat{Q} = [\hat{q}_1, \hat{q}_2, \ldots, \hat{q}_{N_y}]^T$ contains all the wall-normal components, the global matrix $G_{MI} = $ blkdiag$\{c_1 M_1, \ldots, c_{N_y} M_{N_y}\}$, with c_j the coefficient for numerical integration, and $G_{MI}^{1/2}$ is from the Cholesky decomposition of G_{MI}.

In the following, the responses to harmonic and stochastic forcing are accounted for, in turn. A harmonic forcing takes the form $\hat{f}(y, t) = \check{f}(y) \exp(-i\omega t)$, where ω is the circular frequency. After a sufficiently long time, the response is also harmonic as $\hat{q}(y, t) = \check{q}(y) \exp(-i\omega t)$ if the system is linearly stable. From (3.6a–c), the transfer matrix H between $\check{f}$ and $\check{q}$ is

$$\check{q} = H\check{f}, \quad H = (-i\omega I - L)^{-1}, \qquad (3.9a,b)$$

where H is also known as the resolvent. The energy amplification factor between the forcing and the response is defined as $R(\omega, k_x, k_z) = \|\check{q}\|^2 / \|\check{f}\|^2$; then the optimal response is

$$R_{max}(k_x, k_z) = R(\omega_{opt}; k_x, k_z) = \max_{\omega} \frac{\|\check{q}\|^2}{\|\check{f}\|^2} = \|H\|_\infty^2, \qquad (3.10)$$

where ω_{opt} is the optimal frequency. Note that R_{max} is also called the H_∞ norm of the transfer matrix (Zhou, Doyle & Glover 1996). Mathematically, $\|H\|_\infty$ is obtained through a singular value decomposition of H, thus $R_{max} = \sigma_1^2$, where σ_1 is the maximum singular value. Consequently, the relation between $\check{q}$ and $\check{f}$ is

$$\check{q} = \sum_j \sigma_j \cdot (\check{\phi}_j, \check{f})_E \cdot \check{\psi}_j, \qquad (3.11)$$

where $\sigma_1 \geq \sigma_j \geq 0$ are the singular values in descending order, and $\check{\psi}_j$ and $\check{\phi}_j$ are the corresponding response and forcing modes (McKeon & Sharma 2010), respectively, which satisfy the orthogonal relations

$$(\check{\psi}_i, \check{\psi}_j)_E = \delta_{ij}, \quad (\check{\phi}_i, \check{\phi}_j)_E = \delta_{ij}, \qquad (3.12a,b)$$

where δ_{ij} denotes the Kronecker delta. For the optimal response, the unit forcing is $\check{\phi}_1$ and the response is $\check{\psi}_1$. As the channel mean flow is symmetric around the centreline, $\check{\psi}_j$ and $\check{\phi}_j$ are either symmetric or antisymmetric. For the mode of small wavelength, the singular values even appear in pairs (i.e. $\sigma_{2j} = \sigma_{2j-1}$), so the shape function is not unique. For uniqueness, the shape function is normalized such that $\check{u}_1$ is real at its peak amplitude (Moarref *et al.* 2013).

When the system (3.6a–c) is driven by a stochastic forcing, the response is also stochastic. Note that the colour of the nonlinear forcing has been modelled partially by introducing μ_t and Pr_t, so the remaining part of the forcing, i.e. $\hat{f}$ here, is assumed to be white-in-time. Following previous works (e.g. Farrell & Ioannou 1993; Hwang & Cossu 2010b), $\hat{f}$ is a δ-correlated Gaussian white noise process with zero mean:

$$\hat{f} = B\hat{f}_0, \quad \langle \hat{f}_0 \rangle = 0, \quad \langle \hat{f}_0(t_1)\hat{f}_0^H(t_2) \rangle = I \delta_d(t_1 - t_2), \qquad (3.13a–c)$$

where δ_d is the Dirac function, $\hat{f}_0$ is the unmasked forcing, and B is a mask matrix allowing for the calculation of separate responses to different forcing components

(Jovanović & Bamieh [2005](#); Madhusudanan & McKeon [2022](#)). Specifically, B is an identity matrix in normal cases. If, for example, only $\hat{f}_T$ – i.e. the temperature component of the forcing – is considered, then $B = B_T = \text{diag}([0\ 0\ 0\ 0\ 1])$.

The variance of the response $V = \langle\|\hat{q}\|^2\rangle$ is focused on as a measure of energy amplification, where $\langle\cdot\rangle$ denotes the ensemble average. Mathematically, V is also referred to as the H_2 norm of the transfer matrix, representing a temporal integral of $\text{tr}(HH^H)$ in terms of ω (Zhou *et al.* [1996](#)), where $\text{tr}(\cdot)$ is the matrix trace. Equivalently, we have

$$V = \langle \hat{Q}_{MI}^H \hat{Q}_{MI}\rangle = \text{tr}(X_{MI}), \quad X_{MI} = \langle \hat{Q}_{MI}\hat{Q}_{MI}^H\rangle. \tag{3.14a,b}$$

Here, the global covariance tensor X_{MI} is obtained by solving the algebraic Lyapunov equation

$$G_{L,MI}\, X_{MI} + X_{MI}\, G_{L,MI}^H + G_{B,MI}\, G_{B,MI}^H = 0, \quad \langle \hat{Q}\hat{Q}^H\rangle = G_{MI}^{-1/2}\, X_{MI}\, G_{MI}^{-1/2H}, \tag{3.15a,b}$$

where $G_{L,MI} = G_{MI}^{1/2}\, G_L\, G_{MI}^{-1/2}$ and G_L is the global matrix of L, and a similar definition for $G_{B,MI}$. As a result, V is obtained using (3.14a,b) without calculating the temporal integral. We can proceed to solve the eigenvalue problem of $\langle \hat{Q}\hat{Q}^H\rangle$ as

$$\langle \hat{Q}\hat{Q}^H\rangle\, G_{MI}\hat{Y}_j = \theta_j\hat{Y}_j, \tag{3.16}$$

where θ_j and $\hat{Y}_j$ are the eigenvalue and eigenfunction, and $\hat{Y}_j$ satisfies the same orthogonal relation as (3.12a,b). Note that $\hat{Y}_j$ is also called the KL decomposition or the 'proper orthogonal decomposition' mode, representing the leading energy-containing structure of the response. The forcing mode is solved using the back Lyapunov equation. More details can be found in Farrell & Ioannou ([1993](#)), Zhou *et al.* ([1996](#)) and Bamieh & Dahleh ([2001](#)).

The shape function of the harmonic forcing will be denoted as $\hat{q}$ not $\check{q}$ below, where there is no ambiguity. This is intended for consistency with the notation of the stochastic forcing and thus convenience for writing.

3.3. *Numerical consideration*

The procedures in § 3.2 require a discretization in the wall-normal direction. The differential matrices are from the Chebyshev collocation point method (Trefethen [2001](#)). By default, $N_y = 501$ points are used, which is abundant to ensure grid independence (Bae *et al.* [2020b](#)). It is worth mentioning that the c_j for numerical integration come from those of Clenshaw & Curtis ([1960](#)), rather than the direct inverse of the differential matrix, to ensure the positive definiteness of G_{MI}.

The problems of singular value decomposition, Lyapunov equation and eigenvalue, as described in (3.11), (3.15a,b) and (3.16), respectively, are solved using the svd, eig and lyap functions of the Matlab software. In terms of the boundary condition, a no-slip and isothermal wall is assumed on both sides. Therefore, the perturbations at the wall satisfy

$$\hat{u}_w = \hat{v}_w = \hat{w}_w = \hat{T}_w = 0 \quad \text{at } y = \pm 1, \tag{3.17}$$

and $\hat{\rho}_w$ is solved through the perturbed continuity equation. For channel flows, $\hat{\rho}_w$ has the same finite amplitudes at both wall sides, and oscillating unphysical modes may appear. These unphysical modes are recognized and removed in the program as they cannot converge with increasing N_y (Bewley & Liu [1998](#)). Verification of the linear response solvers with previous results is provided in Appendix B.
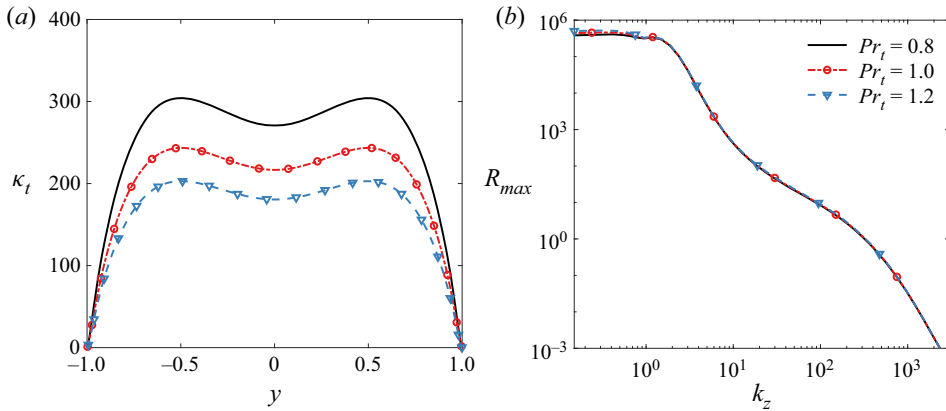
Figure 3. (*a*) Eddy thermal conductivity and (*b*) energy amplification factor of the optimal harmonic response ($k_x = 0$) based on the mean flow of different turbulent Prandtl number. The case parameters are $Ma_b = 4$ and $Re_\tau = 6000$.

3.4. *Eddy viscosity and thermal conductivity*

If the turbulent statistics are not available, then μ_t can be evaluated from the mean streamwise momentum (2.1*b*) as

$$0 = -\frac{d\bar{P}}{dx} + \frac{d}{dy}\left[(\bar{\mu} + \mu_t)\frac{d\bar{U}}{dy}\right] \quad \rightarrow \quad \mu_t = \frac{1 - y^+/Re_\tau}{d\bar{U}^+/dy^+} - \bar{\mu}, \qquad (3.18)$$

the same as that in (2.7). For Pr_t, its expression by definition is

$$Pr_t = \frac{\overline{\widetilde{u}\widetilde{v}}\, \partial \bar{T}/\partial y}{\overline{\widetilde{v}\widetilde{T}}\, \partial \bar{U}/\partial y}, \qquad (3.19)$$

which is shown to be approximately unity in most regions in the channel flow (Huang *et al.* 1995; Modesti & Pirozzoli 2016). Therefore, Pr_t can be assumed to be simply a constant. The linear response results of different Pr_t are compared below.

To highlight the influence of Pr_t, the case of a relatively high Ma_b of 4 is selected, and $Re_\tau = 6000$. Figure 3(*a*) gives the distribution of κ_t with $Pr_t = 0.8$, 1.0 and 1.2, respectively. Despite the relatively large difference in Pr_t, the amplification factor of the optimal harmonic response is little affected, as shown in figure 3(*b*). A visible difference exists only in the region $k_z h < 1$. The same conclusion applies to the stochastic response (not shown here). For the convenience of calculation, $Pr_t = 1$ is selected for later use.

3.5. *Linear response calculation based on the ODE solver*

Although the ODE solver can provide an accurate mean flow, the corresponding linear response results may have large deviations from those using the DNS mean flow since there are first- and second-order derivatives of the mean flow in (3.4). Here, the reliability of the ODE-based mean flow in predicting the linear response is examined further.

Two representative cases are selected. The first is the incompressible $Re_\tau = 5200$ case from Lee & Moser (2015), whose Re_τ is very high for a channel flow. This helps to examine the present solver when extended to the high-Reynolds-number regime. Note that Ma_b is set to 0.01 in the present solver for this case, to avoid singularities. The second case
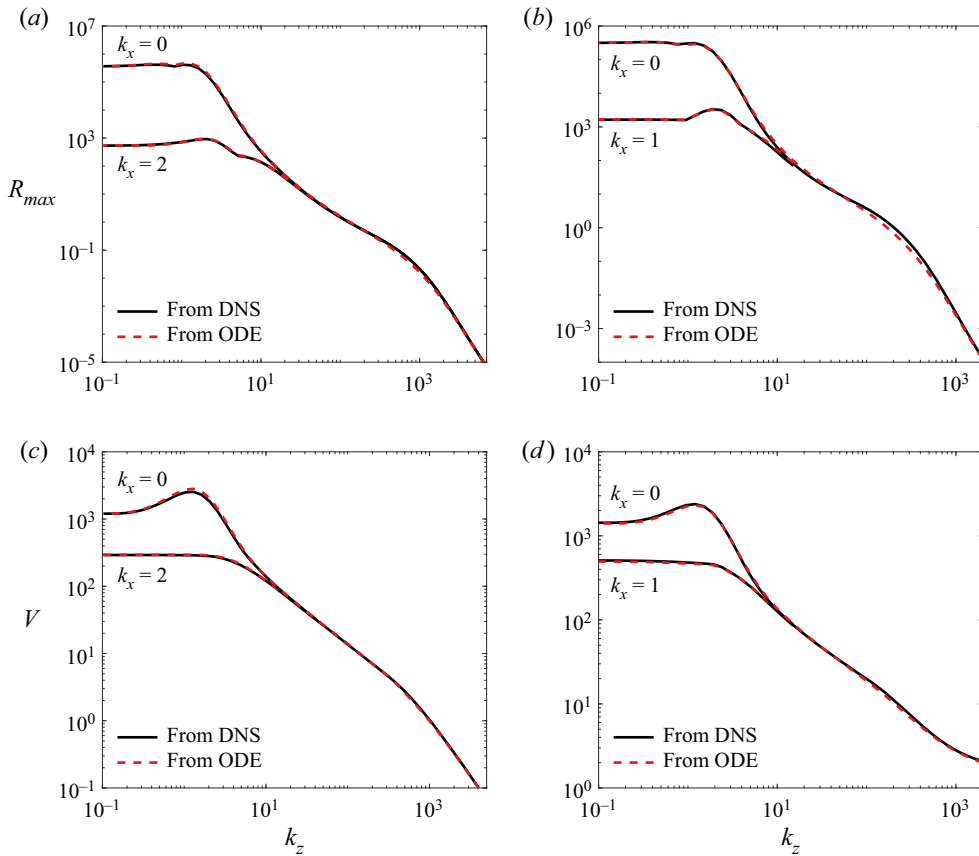
962 A7-14

Figure 4. Energy amplification factors of the (a,b) optimal harmonic and (c,d) stochastic forcing based on the mean flows from DNS and the ODE solver. Two cases are (a,c) the $Re_\tau = 5200$ case from Lee & Moser (2015), and (b,d) the $Ma_b = 1.5$, $Re_\tau = 1910$ case from Yao & Hussain (2020).

is the $Ma_b = 1.5$, $Re_\tau = 1910$ case from Yao & Hussain (2020) (no. (15) in table 2 in Appendix A), which has both a high Re_τ and obvious compressibility effects. The energy amplification factors of both optimal harmonic and stochastic responses for the two cases are plotted in figure 4. As can be seen, the results based on the mean flow from the ODE solver match well with those using the DNS mean flow. A small visible difference exists near $k_z h \sim 10^2$ in figure 4(*b*). This is attributed to the difference of $\bar{U}$ at the junction of the buffer and logarithmic layers, which originates from the deviation of the incompressible curve fit in (2.7) (see Appendix A for more details). In short, figure 4 demonstrates the reliability of the present ODE solver in calculating the linear response of the turbulent mean flow.

4. Results and discussions

4.1. *Basic characteristics of responses*

The basic characteristics of the responses to the harmonic and stochastic forcing are analysed first. The case parameters are selected to be $Ma_b = 2.0$ and $Re_\tau = 6000$, which is a benchmark case in this work. A parameter study will be conducted in § 4.3.
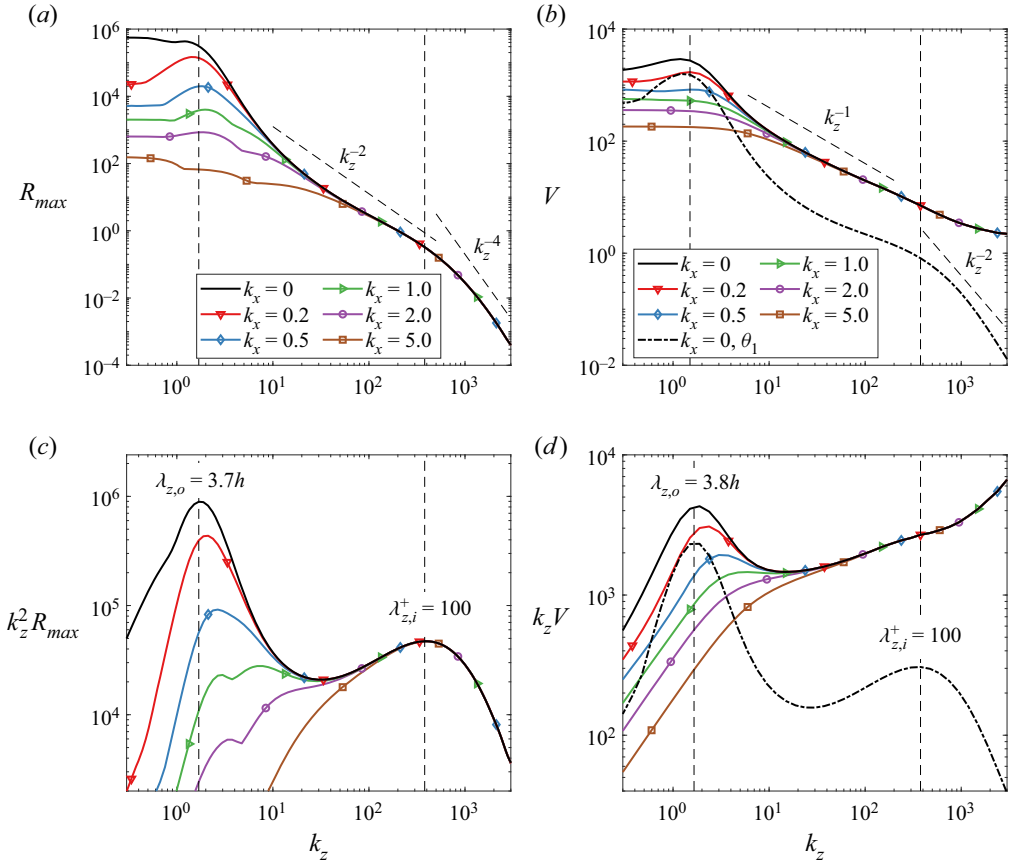
Figure 5. (*a*,*b*) Energy amplification factors, and (*c*,*d*) corresponding pre-multiplied factors of the (*a*,*c*) optimal harmonic and (*b*,*d*) stochastic forcing in the $Ma_b = 2$, $Re_\tau = 6000$ case.

First, the curves of R_{max} and V with different k_x and k_z are plotted in figures 5(*a*) and 5(*b*). An overall feature is that the R_{max} and V values in the large-scale region (in terms of the spanwise wavelength $\lambda_z = 2\pi/k_x$) are orders of magnitude higher than those in the small-scale region, reflecting the energetic nature of the former (Kim & Adrian 1999). Meanwhile, R_{max} and V of the large-scale motion are strongly dependent on k_x when $\lambda_z > 0.3h$. The modes with the largest R_{max} and V both have an infinite streamwise wavelength (i.e. $k_x = 0$); for the harmonic forcing, the most amplified mode is also steady ($\omega_{opt} = 0$). In contrast, R_{max} and V in the small-scale region are very insensitive to k_x, where the curves of different k_x nearly collapse with each other.

Hwang & Cossu (2010*b*) found, in their incompressible flow case, that there exist a k_z^{-2} scaling and a k_z^{-1} scaling in the mid-k_z range for R_{max} and V, respectively. We also apply these scalings for the compressible case here for examination. A theoretical analysis on the linear operator related to these scalings will be provided in §5. The pre-multiplied energy amplification factors $k_z^2 R_{max}$ and $k_z V$ are plotted in figures 5(*c*) and 5(*d*). The variation of $k_z^2 R_{max}$ bears a strong resemblance to that in the incompressible case, where the classic bimodal structure is observed (del Álamo & Jiménez 2006; Cossu *et al.* 2009). These two peaks correspond to the large-scale motions in the outer layer (termed 'outer peak') and the small-scale motions in the near-wall region (termed 'inner peak'),

respectively, as also noted by Alizard *et al.* (2015) using the transient growth analysis. The λ_z^+ of the inner peak, denoted $\lambda_{z,i}^+$, is approximately 100, while the λ_z of the outer peak, denoted $\lambda_{z,o}$, decreases with k_x rise and has maximum value approximately $3.7h$ at $k_x = 0$. For $k_z V$, it also peaks near $\lambda_{z,o} = 3.8h$ in the large-scale region, but exhibits distinct features from the incompressible case in the small-scale region (see figure 19(*b*) in Appendix B for reference). The slope of V does not decrease but increases at $k_z h > 400$, so the inner peak is missing in $k_z V$. For reference, the variations of θ_1 and $k_z \theta_1$ are also plotted in figures 5(*b*) and 5(*d*). As stated in § 3.2, θ_1 is the largest eigenvalue of the covariance matrix, and represents the mode that receives the largest energy gain. As can be seen, $k_z \theta_1$ has the same trend of variation as $k_z V$ in the large-scale region, but exhibits the inner peak in the small-scale region. In addition, the inner peak also locates at approximately $\lambda_z^+ = 100$, very close to that of $k_z^2 R_{max}$. The different behaviour of $k_z V$ here from the incompressible case indicates that the compressibility effects can be the cause. This is discussed further below.

The mask matrix $\boldsymbol{B}$ (see (3.13*a–c*)) is used to study the responses to different forcing components. Therefore, $\boldsymbol{B}$ is separated into two parts, i.e. the kinematic part and the thermodynamic part (Madhusudanan & McKeon 2022), as

$$\boldsymbol{B} = \boldsymbol{B_u} + \boldsymbol{B_{\rho T}}, \quad \boldsymbol{B_u} = \text{diag}([0\ 1\ 1\ 1\ 0]), \quad \boldsymbol{B_{\rho T}} = \text{diag}([1\ 0\ 0\ 0\ 1]). \quad (4.1a\text{–}c)$$

The variances of the responses to the two forcing parts are denoted $V_{\boldsymbol{u}}$ and $V_{\rho T}$, respectively. By definition, $V_{\boldsymbol{u}}$ results from the forcing applied only to three velocity equations, i.e. $\hat{f}_\rho = \hat{f}_T = 0$, the same as that in an incompressible flow. Likewise, $V_{\rho T}$ results from the forcing components present only in the density and temperature equations, i.e. $\hat{f}_u = \hat{f}_v = \hat{f}_w = 0$. It is worth mentioning that $\hat{f}_T = 0$ does not mean $\hat{T} = 0$ because of the variable coupling. Figure 6(*a*) gives the distribution of V, $V_{\boldsymbol{u}}$ and $V_{\rho T}$. Approximate linear superposition $V \approx V_{\boldsymbol{u}} + V_{\rho T}$ is satisfied with relative error less than 2 %. The shape of $k_z V_{\boldsymbol{u}}$ is quite similar to that in the incompressible flow (see figure 19 for reference). It tends to decrease at $k_z h > 400$, so the inner peak related to the near-wall motion can be recognized, also located at $\lambda_z^+ \approx 100$. In comparison, $k_z V_{\rho T}$ increases monotonically with k_z. It is one order of magnitude smaller than $k_z V_{\boldsymbol{u}}$ around the outer peak, but rises to be the larger one with k_z higher than the inner peak ($\lambda_z^+ < 100$), which results simultaneously in the quick increase of $k_z V$. Therefore, it is the thermodynamic part of the forcing – i.e. the components in the equations of $\hat{\rho}$ and $\hat{T}$ – that leads to the different trend of $k_z V$ in the compressible flow case.

Furthermore, the KL modes of the three covariance tensors corresponding to V, $V_{\boldsymbol{u}}$ and $V_{\rho T}$ are computed to see the contribution from the most energetic modes. The contribution is measured by the ratio $r_V = (\theta_1 + \theta_2)/V$. The second mode ($\theta_2$) is also included because in the small-λ_z region, the θ_j appear in pairs, i.e. $\theta_1 = \theta_2$. As shown in figure 6(*b*), the two maxima of $r_{V_{\boldsymbol{u}}}$ are 89 % and 42 %, near the outer and inner peaks, respectively, indicating that a large portion of $V_{\boldsymbol{u}}$ is contributed by one mode pair (or two modes). This energetic mode is representative in describing the local turbulent characteristics. In comparison, $r_{V_{\rho T}}$ decreases continuously with k_z, and is less than 3 % at $k_z h > 380$ ($\lambda_z^+ < 100$). This suggests that no single mode dominates in terms of the energy contribution, i.e. the response is of little coherence in the small-λ_z region, though $V_{\rho T}$ is large. As $r_{V_{\boldsymbol{u}}}$ is much larger than $r_{V_{\rho T}}$, $\theta_{1,\boldsymbol{u}}$ dominates $\theta_{1,\rho T}$ in most regions. Therefore, θ_1 nearly equals $\theta_{1,\boldsymbol{u}}$, or in other words, the most energetic mode to the total variance is contributed mainly by $\theta_{1,\boldsymbol{u}}$. The r_V at the outer and inner peaks are 81 % and 21 %, respectively, pulled down by $r_{V_{\rho T}}$. The above comparison demonstrates clearly the distinct feature between the responses to
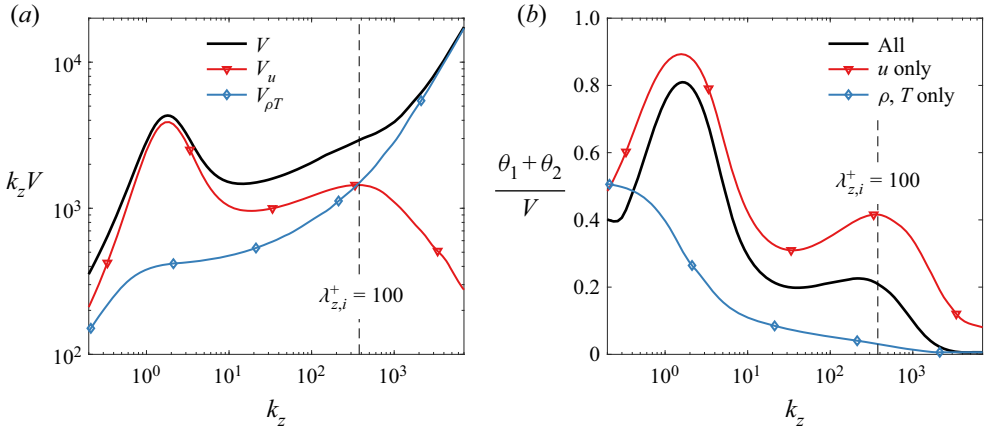
Figure 6. (*a*) Pre-multiplied energy growth factors, and (*b*) contribution of the two most energetic KL modes of the stochastic response to different forcing components ($k_x = 0$).

the kinematic and thermodynamic components of the forcing. The former is analogous to the incompressible counterpart, exhibiting characteristic large- and small-scale motions. The latter significantly affects the small-scale motion, and is of little coherence.

4.2. *Response structure*

The shape functions of the modes at the outer and inner peaks ($k_x = 0$) in figure 5 are plotted in figure 7, where both the response and forcing are provided. The wall-normal and spanwise velocities are the two largest components in the input signal, and so are the streamwise velocity and temperature components in the output signal. One significant feature is that the shape functions of the optimal harmonic and stochastic forcing/response are nearly identical, in both shape and amplitude, as also noted by Hwang & Cossu (2010*b*) in the incompressible case. This is because $\hat{q}$ of the harmonic response is very insensitive to ω at $k_x = 0$, so $\hat{q}$ is nearly unchanged from a harmonic forcing to a broadband stochastic one. From a physical point of view, the convection term $\bar{U} \cdot \nabla \hat{q}$ vanishes with $k_x = 0$, hence the response shape is determined primarily by the local mean-flow gradient. In terms of different components, the peak locations of $|\hat{v}|$ and $|\hat{w}|$ are different, forming a streamwise vortex to be shown later. The maxima of $|\hat{u}|$ and $|\hat{T}|$ of the inner-peak mode are at $y^+ = 11$ and $y^+ = 10$, both of which lie within the buffer layer. For the outer-peak mode, both $\hat{u}$ and $\hat{T}$ penetrate deep into and below the logarithmic region, as labelled by the dashed line at $y^+ = 100$ in figure 5(*d*) (recall that $Re_\tau = 6000$). This is indicative of an amplitude modulation effect of the outer-layer motions on the near-wall velocity and temperature (Marusic *et al.* 2010*a*; Cheng, Shyy & Fu 2022; Yu & Xu 2022). Specifically, the forcing imposed in the outer region (especially $\hat{v}$) induces large amplitudes of streamwise velocity and temperature near the wall as the response. Meanwhile, $\hat{T}$ penetrates deeper towards the wall than $\hat{u}$, owing to the relatively large temperature gradient near the wall.

As discussed in figure 6, the most energetic modes at the outer and inner peaks result mainly from the kinematic parts of the forcing. In this sense, $\hat{T}$ behaves more like a passive scalar (noted by Coleman *et al.* 1995), resulting from the interaction between velocity components of the forcing and the mean temperature gradient. This is demonstrated in
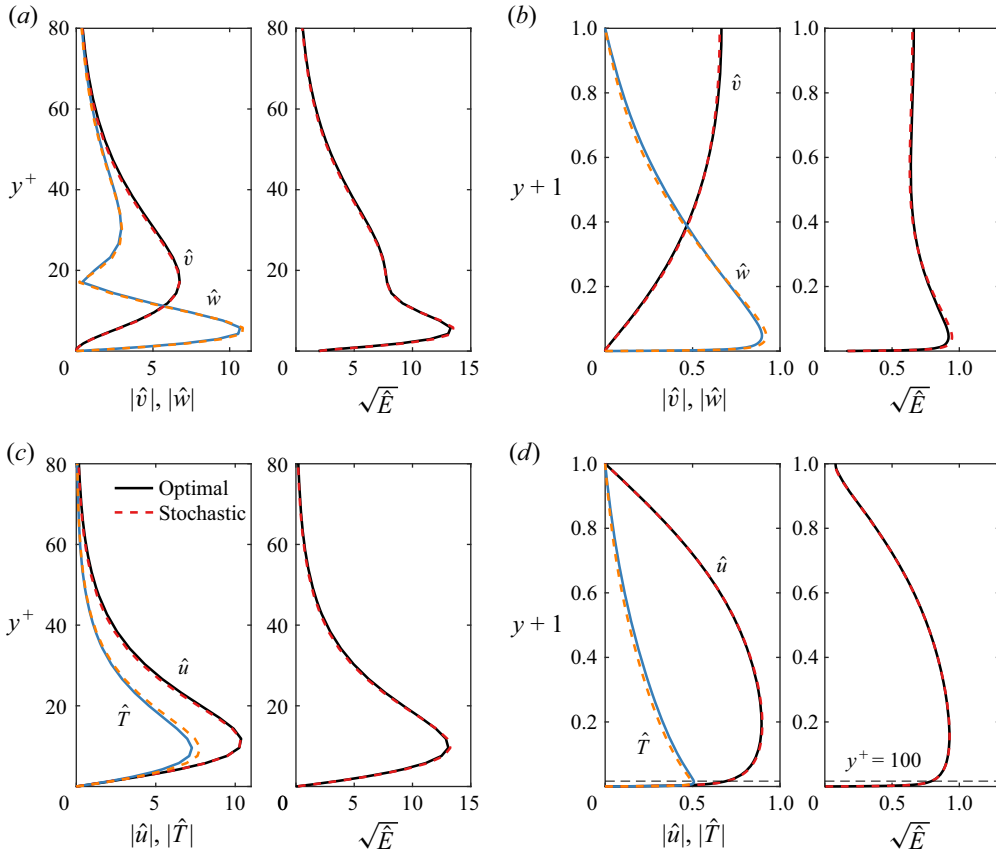
Figure 7. Shape functions of different components and the energy norm of the (*a*,*b*) forcing and (*c*,*d*) response at $k_x = 0$ for the mode at the (*a*,*c*) inner peak ($\lambda_z^+ = 100$) and (*b*,*d*) outer peak ($\lambda_z = 3.7h$) in figure 5.

figure 8, where the contours of $\tilde{u}$ and $\tilde{T}$ in the y–z plane are depicted for optimal harmonic response. The shape of the stochastic response is nearly the same (see figure 7) and is thus not shown here. The velocity vector $[\tilde{w}, \tilde{v}]$ of the forcing is also plotted to identify the in-plane motion. As can be seen, the classic combination of quasi-streamwise vortices and streamwise streaks is recognized for the modes of both inner and outer peaks. Moreover, the streamwise vortex as the input strongly promotes the streaks of streamwise velocity and temperature as the output through the lift-up effect (Ellingsen & Palm 1975; Schoppa & Hussain 2002). For both modes here, the temperature streaks look more stuck to the wall, as already shown in figure 7.

More discussion is provided on the structure of the outer-peak mode. As shown in figures 8(*c*) and 8(*d*), the contour of the response almost fills in the whole spatial domain, and extends to as long as $\lambda_{z,o} = 3.7h$ in the spanwise direction. This value is very close to that in incompressible channel flows (e.g. Cossu *et al.* 2009; Pujals *et al.* 2009). Actually, as will be shown in § 4.3, $\lambda_{z,o}$ is nearly independent of Ma_b and Re_τ, standing as a pretty robust feature of the optimal response in the outer layer. However, as noted by previous researchers, such a large-scale structure has not been observed in the DNS data or the experiment. The outer peak of the pre-multiplied energy spectra from DNS indicates a
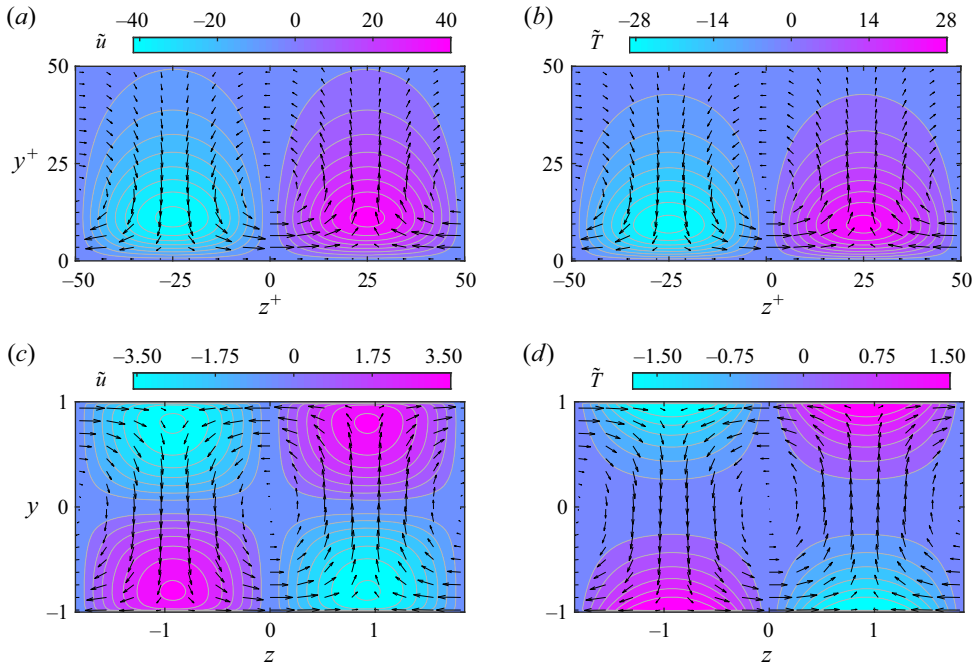
Figure 8. Contours of the (*a,c*) streamwise velocity and (*b,d*) temperature of the optimal harmonic response for the modes of the (*a,b*) inner peak ($\lambda_z^+ = 100$) and (*c,d*) outer peak ($\lambda_z = 3.7h$) in the *y–z* plane. The velocity vector is based on the spanwise and wall-normal velocities of the forcing.

spanwise scale $\lambda_z \approx h - 2h$ for both incompressible (Lee & Moser 2015) and compressible (Yao & Hussain 2020) channel flows. Part of the reason is that the structures in figure 8 correspond to infinite λ_x ($k_x = 0$), but in actual flows it is hard to extend to that long. According to figure 5(*c*), $\lambda_{z,o}$ decreases at a lower λ_x, to be closer to the DNS data. In addition, nonlinear effects of the response growth can also lead to the difference (Cossu *et al.* 2009).

In the incompressible flow case, the $\hat{u}$ response with different k_z values between those of the inner and outer peaks exhibits a geometrically self-similar structure (Pujals *et al.* 2009; Hwang & Cossu 2010*b*; McKeon 2019). Specifically, the normalized $|\hat{u}|$ of different k_z can be collapsed approximately using a wall-normal coordinate y^+/λ_z^+. The amplitude peaks lie within the logarithmic layer, so this self-similar structure stands as a supporting proof for the well-known AEM (Townsend 1976). In addition, the outer-layer large-scale motions and near-wall small-scale motions can be regarded as the largest and smallest attached eddies, respectively (Hwang 2015; Cheng *et al.* 2019, 2022). Although abundant evidence has appeared to support the AEM in the incompressible turbulence, its behaviour and validity in compressible turbulence are far from clear. Here, we provide some understanding of the compressible AEM by examining the geometrical self-similarity of the response.

The streamwise velocity, temperature and energy norm of the optimal harmonic response are plotted in figure 9, with λ_z^+ ranging from 800 to 4000 ($\lambda_z/h = 0.13 - 0.67$). They all exhibit a streamwise-elongated streaky structure, as observed in the high-speed experiment (Ganapathisubramani, Clemens & Dolling 2006). The peaks of $|\hat{u}|$ of these modes lie within the logarithmic layer, but those of $|\hat{T}|$ are much closer to the wall due to large mean temperature gradient there. To collapse the highly scattering distribution of the
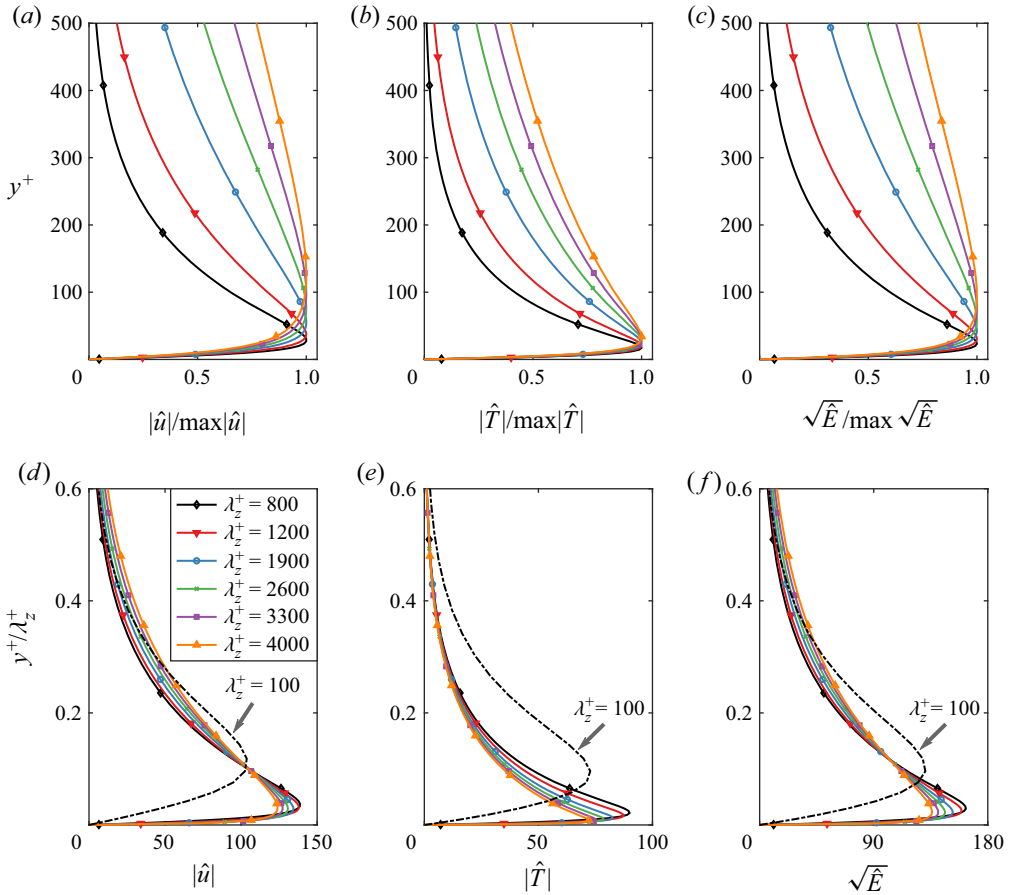
962 A7-20

Figure 9. Wall-normal distribution of the (*a*,*d*) streamwise velocity, (*b*,*e*) temperature, and (*c*,*f*) energy norm for the optimal harmonic response ($k_x = 0$) with different spanwise wavelengths. The black dashed lines are the corresponding results of the $\lambda_z^+ = 100$ mode. The coordinates in (*d–f*) are normalized by the spanwise wavelength.

shape function, the wall-normal coordinate y^+ is normalized by λ_z^+. As the amplitude of $\hat{q}$ is determined by (3.12*a*,*b*) based on the integral form in (3.7), the amplitude is normalized correspondingly using λ_z^+. As shown in figures 9(*d*)–9(*f*), the normalized curves of different λ_z^+ are much more concentrated, and are collapsed to a first approximation. Also, the maximum of the normalized $|\hat{T}|$ experiences larger variations with λ_z^+ than those of $|\hat{u}|$ and $\hat{E}$. For comparison, the shapes of the inner-peak mode ($\lambda_z^+ = 100$), as shown in figure 7, are also plotted in black dashed lines. As can be seen, the curve of $\lambda_z^+ = 100$ apparently deviates from others of higher λ_z^+. This is reasonable because its amplitude peak is already within the buffer layer (see figure 7), out of the logarithmic region, which violates the assumptions of the AEM. Another wall-normal coordinate widely used in compressible turbulence is the semi-local one, y^*. But here, the ratio y^*/λ_z^* equals y^+/λ_z^+, thus leading to no difference in collapsing curves. As the unit δ_ν^* and thus λ_z^* are not invariant at different y^+, other attempts at normalization can be deployed to reflect the difference between y^+ and y^*. For example, $\lambda_z^*(y^+)$ can be replaced with
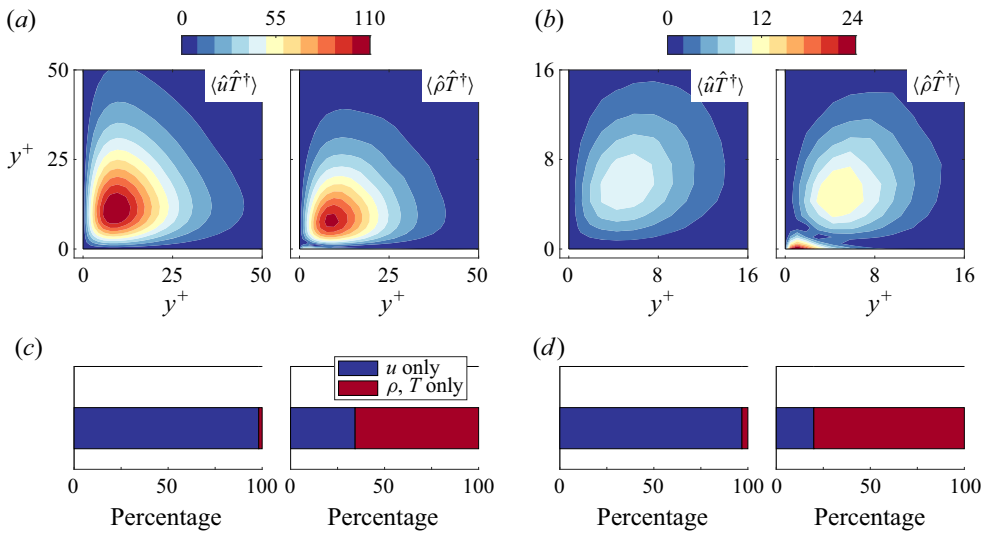
Figure 10. (*a,b*) Component cospectrum in the y^+–y^+ plane, and (*c,d*) the relative contribution from the response to different components of the forcing. The two y^+ in the horizontal and vertical coordinates in (*a,b*) are for the two variables in $\langle \cdot \rangle$, respectively. The response mode is $k_x = 0$, with (*a,c*) $\lambda_z^+ = 100$ and (*b,d*) $\lambda_z^+ = 20$. Each pair of plots (contour and bar) in (*a,c*) and (*b,d*) represents the same variable as labelled.

$\lambda_z^*(y_m^+)$, where y_m^+ is a fixed point for each λ_z^+. As a choice of y_m^+, the peak location of $|\hat{u}|$ (or $|\hat{T}|$, $\hat{E}$), denoted $y_{U_m}^+$, can be regarded as a characteristic wall-normal scale of the response. Nevertheless, using $y^*/\lambda_z^*(y_{U_m}^+)$ as the wall-normal coordinate results in no visible improvement in collapsing curves (hence not shown here).

Finally, the response modes of $\lambda_z^+ < 100$ are focused on because they have different behaviours from the incompressible case (see figure 6). Figures 10(*a*) and 10(*b*) display two representative cospectra, $\langle \hat{u}\hat{T}^\dagger \rangle$ and $\langle \hat{\rho}\hat{T}^\dagger \rangle$, for the modes of $\lambda_z^+ = 100$ and $\lambda_z^+ = 20$, respectively. The cospectrum is obtained by extracting the sub-elements of $\langle \hat{q}\hat{q}^H \rangle$ in (3.15*a,b*). Moreover, to study the contributors to these cospectra, the responses to the kinematic and thermodynamic parts of the stochastic forcing are calculated separately, denoted as $\langle \hat{q}\hat{q}^H \rangle_u$ and $\langle \hat{q}\hat{q}^H \rangle_{\rho T}$, respectively. Their relative contributions to the cospectrum are plotted in figures 10(*c*) and 10(*d*) in percentages. As can be seen, over 95 % of $\langle \hat{u}\hat{T}^\dagger \rangle$ is contributed by $\langle \hat{u}\hat{T}^\dagger \rangle_u$ for both modes, indicating the strong coupling between the streaks of streamwise velocity and temperature induced by the streamwise vortices as shown in figure 8. On the other hand, the contribution from the thermodynamic part of the forcing is negligible. With λ_z^+ decreasing, the amplitude of $\langle \hat{u}\hat{T}^\dagger \rangle$ quickly diminishes (see figure 6), to less than half of $\langle \hat{\rho}\hat{T}^\dagger \rangle$ at $\lambda_z^+ = 20$. This is reasonable because as the streak motion is closer to the wall, the $\hat{v}$ component is restricted by the wall boundary, thus the streamwise vortex is suppressed. Compared with $\langle \hat{u}\hat{T}^\dagger \rangle$, $\langle \hat{\rho}\hat{T}^\dagger \rangle$ has two hot zones. One is around the buffer layer as well, resulting from the coupling of the temperature and density streaks. The other is attached to the wall within the viscous layer, contributed mainly by $\langle \hat{\rho}\hat{T}^\dagger \rangle_{\rho T}$. As shown in figure 6, the response of the second hot zone is of little coherence, and is connected to the large mean density gradient there through the perturbed
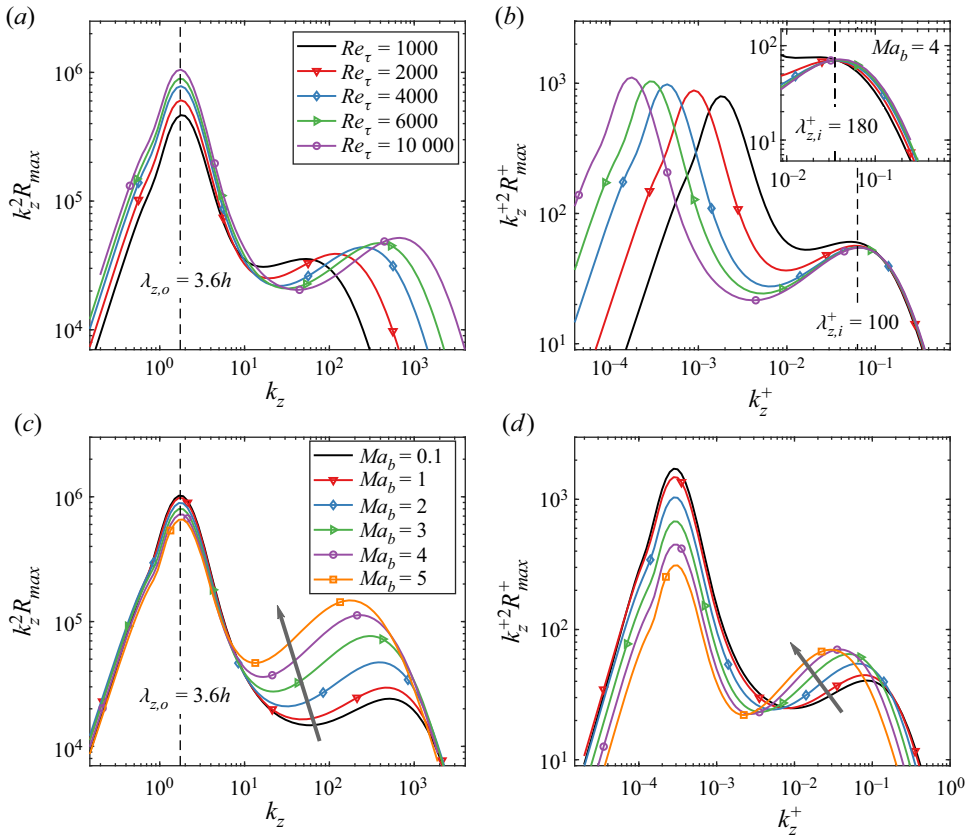
962 A7-22

Figure 11. Pre-multiplied energy amplification factors of the optimal harmonic responses ($k_x = 0$) for the cases with (a,b) different Re_τ ($Ma_b = 2$), and (c,d) different Ma_b ($Re_\tau = 6000$). Plots (a,c) are in the outer units, and (b,d) are in the inner units. Note that the inset in (b) gives the same results as (b) except that $Ma_b = 4$.

continuity equation. With λ_z^+ decreasing from 100 to 20, the peak amplitude of $\langle \hat{\rho}\hat{T}^\dagger \rangle$ shifts to the wall, reflecting the strengthening of the relative importance of $\langle \hat{q}\hat{q}^H \rangle_{\rho T}$.

4.3. *Effects of Reynolds and Mach numbers*

The cases of different Ma_b and Re_τ are investigated further, with an emphasis on compressibility effects. Figure 11 depicts the energy amplification factors of the optimal harmonic responses for different cases. Both the outer and inner units are deployed to study the characteristics of the outer and inner peaks. For the outer-region motion, one significant feature from figures 11(a) and 11(c) is that the outer peaks all correspond to $\lambda_{z,o} \approx 3.6h$ for different Re_τ and Ma_b. Here, Re_τ is from 10^3 to 10^4, and Ma_b is from 0.1 to 5, both covering a relatively large range. The weak dependence of $\lambda_{z,o}$ on Re_τ has already been reported in previous research (see e.g. Pujals *et al.* 2009), attributed to the fact that the large-scale motion in the outer layer cannot directly 'feel' the presence of the wall, and is hence least affected (Pirozzoli 2014). Furthermore, the weak dependence of $\lambda_{z,o}$ on Ma_b is demonstrated in the present work. This trend is consistent with the observation in experiment (Spina *et al.* 1994; Williams *et al.* 2018) and from DNS of the energy spectrum at different Ma_b (Modesti & Pirozzoli 2016; Yao & Hussain 2020; Cogo *et al.* 2022; Cheng
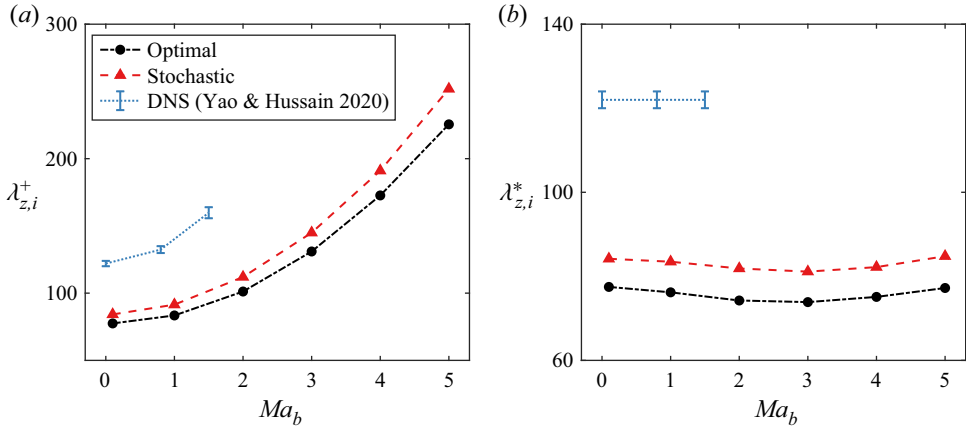
Figure 12. Variation of the spanwise wavelength of the inner-peak mode with Ma_b, expressed using the (*a*) inner units and (*b*) semi-local units for both the optimal harmonic and stochastic responses. The results evaluated from the DNS energy spectra at $y^* = 15$ are also plotted (Yao & Hussain 2020).

& Fu 2022*b*). As discussed in figure 6, the large-scale structure corresponding to the outer peak results mainly from the kinematic part of the forcing, not the thermodynamic part. Thereby, its motion nature can partly explain the weak dependence on Ma_b.

For the mode of the inner peak, it is observed that the pre-multiplied energy growths of different Re_τ are nearly collapsed using the inner units for the Mach 2 case (see figure 11*b*), where $\lambda_{z,i}^+ \approx 100$. This collapse is also achieved when Ma_b is increased to 4, as displayed in the inset, except that $\lambda_{z,i}^+$ rises to 180. Actually, $\lambda_{z,i}^+$ indeed increases with Ma_b, as shown in figure 11(*d*). Meanwhile, with the increase of Ma_b, the k_z^{-2} scaling of R_{max} in the mid-k_z range has more significant deviations, and $k_z^2 R_{max}$ of the inner peak rises in both outer and inner units. This trend will be discussed further in § 5 by analysing the perturbation equations. Through a comparison with the $k_z^2 R_{max}$ of the outer peak, the relative importance of the near-wall motion is enhanced, in terms of amplifying the response energy.

The variation of $\lambda_{z,i}^+$ with Ma_b is further quantified, as depicted in figure 12(*a*). The $\lambda_{z,i}^+$ evaluated from $k_z^+ \theta_1^+$ of the stochastic response is also plotted. As discussed in figure 5, the variation of $k_z \theta_1$ bears a strong resemblance to $k_z^2 R_{max}$. It is observed that $\lambda_{z,i}^+$ increases by over three times with Ma_b lifted up from 0.1 to 5, whether evaluated from $k_z^+ \theta_1^+$ or $k_z^{2+} R_{max}^+$. As noted in § 2.2, the increase of Ma_b results simultaneously in a wall-cooling effect for the channel flow. Wall cooling is shown in the DNS results to rapidly increase the spanwise spacing of the near-wall streaks for both boundary-layer and channel flows (Morinishi *et al.* 2004; Duan *et al.* 2010; Zhang *et al.* 2022), consistent with the trend in figure 12(*a*). For more quantitative comparison, available DNS results of channel flows are added. The data are from Yao & Hussain (2020) with a maximum Ma_b of 1.5. The $\lambda_{z,i}^+$ plotted are calculated from the local maximum of their pre-multiplied energy spectra of the streamwise velocity at a fixed $y^* = 15$. As the spectra data are not publicly available, the points are evaluated by the present authors from their published figures, so error bars are added to display the potential error. There is a systematic difference between the $\lambda_{z,i}^+$ from the linear response analysis and the DNS results, which has also been noted and interpreted in previous research, and will be discussed at length later.
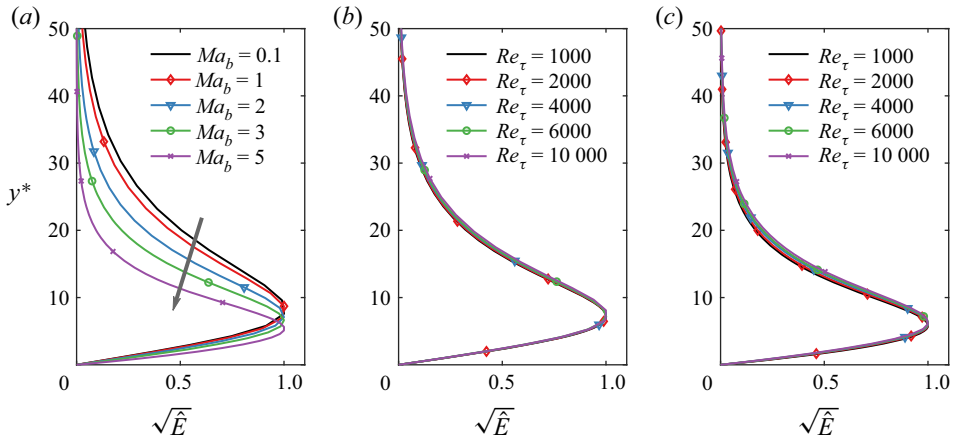
962 A7-24

Figure 13. Wall-normal distributions of the normalized energy norm of the inner-peak mode for the cases (a) $Re_\tau = 6000$ and varying Ma_b, (b) $Ma_b = 2$ and varying Re_τ, and (c) $Ma_b = 4$ and varying Re_τ.

As demonstrated by Yao & Hussain (2020), if expressed using semi-local units, $\lambda^*_{z,i}$ values are all approximately 120 for the three cases with varying Ma_b. To apply this scaling, the wall-normal height to determine δ^*_v is selected to be $y^+_{E_m}$, i.e. the peak location of $\hat{E}$, as introduced in §4.2. The resulting variation of $\lambda^*_{z,i}$ with Ma_b is plotted in figure 12(b). It is observed that both $\lambda^*_{z,i}$ from the optimal and stochastic responses are nearly invariant with Ma_b up to 5, consistent with the trend in the DNS data in terms of the spanwise spacing of the near-wall streaks (Morinishi *et al.* 2004; Patel *et al.* 2016; Zhang *et al.* 2022). Nevertheless, the current DNS database of channel flows cannot reach a Ma_b as high as 5. In this sense, the result in figure 12(b) is predictive, waiting for more reference points at higher Ma_b for further examination. From the variation of δ^*_v, it is conjectured that the increase of $\lambda^+_{z,i}$ with Ma_b rise is due mainly to the $\bar{T}/T_w$ increase, or equivalently the $\bar{\rho}/\rho_w$ decrease.

More discussion is provided on the systematic deviation of $\lambda^+_{z,i}$ and $\lambda^*_{z,i}$ in figure 12 from the DNS data. The first reason is that only the principal mode (pair) is considered here. Though it explains a large portion of the total energy amplification (see figure 6), secondary modes may also play crucial roles. An approach for improvement is to consider several leading modes, such as the work by McMullen *et al.* (2020), which impressively reproduced the energy spectra in an incompressible case. However, the determination of weights for different modes involves the usage of instantaneous DNS data, which limits the prediction capability, especially for compressible flows. Second, the energy amplification factor in figure 11 at a given (k_x, k_z, ω) is a global measure of the response at all wall-normal heights, so it is not a direct analogy to the energy spectra in the DNS, which is fixed at a specific height. As noted by Cossu *et al.* (2009), the $\lambda^+_{z,i}$ of the inner peak denotes the 'most probable' value of the spanwise spacing, while that from DNS is more like a 'mean' value.

The energy norm of the inner-peak mode is displayed in figure 13 for the cases of varying Re_τ and Ma_b. The usage of $\hat{E}$ is a universal measure of the response structure rather than $\hat{u}$ or $\hat{T}$ alone across different Ma_b. As discussed in figure 12, y^* is used for $\hat{E}$ of various Ma_b, and hence also for the cases of varying Re_τ for consistency. As can be seen, the $\hat{E}$
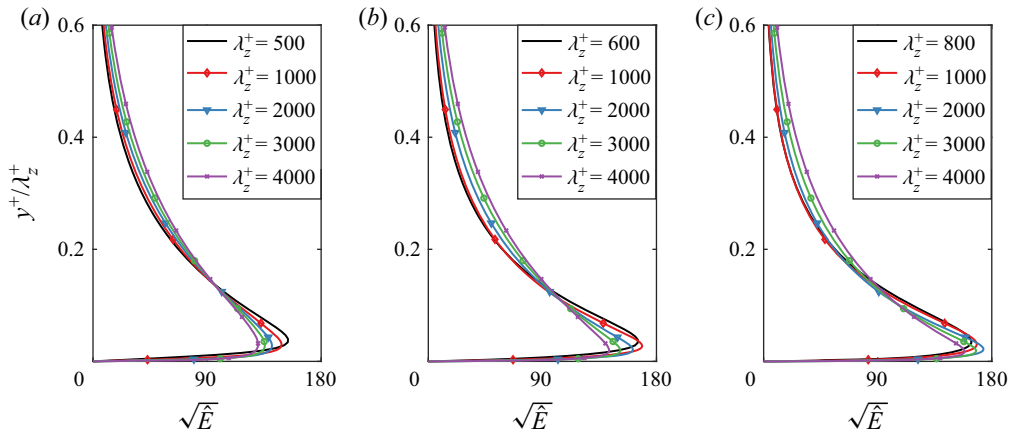
Figure 14. Wall-normal distributions of the normalized energy norm for the cases with $Re_\tau = 6000$ and (*a*) $Ma_b = 0.1$, (*b*) $Ma_b = 3$, and (*c*) $Ma_b = 5$, for the optimal harmonic response ($k_x = 0$) with different spanwise wavelengths.

profiles of different Re_τ are nearly collapsed in figures 13(*b*) and 13(*c*). In comparison, the $\hat{E}$ profiles of different Ma_b exhibit visible differences; $y_{E_m}^+$ decreases continuously with Ma_b rises, which is due to the increasingly large temperature gradient of the mean flow.

The geometrical self-similarity of the response in the mid-k_z range has been discussed in § 4.2 for the case $Ma_b = 2$. Here, the self-similar characteristics are examined further for the cases of different Ma_b. Figure 14 gives the normalized energy norms of different λ_z^+ with $Ma_b = 0.1$, 3 and 5, in the same style as in figure 9. The minimum λ_z^+ displayed increases from 500 to 800 with Ma_b rise because, as shown in figure 9, the mode with λ_z^+ close to $\lambda_{z,i}^+$ has obvious deviations, and $\lambda_{z,i}^+$ increases at a higher Ma_b (see figure 12*a*). As can be seen, the energy norms of different λ_z in the mid-λ_z range all approximately collapsed with Ma_b ranging from 0.1 to 5. The above observation demonstrates that the geometrical self-similarity of the response is little influenced by the compressibility effect, which is helpful in understanding the AEM for supersonic flows.

As shown in figure 6, $V_{\boldsymbol{u}}$ and $V_{\rho T}$ have totally different behaviours at different k_z. Their variations with Ma_b are investigated further, as plotted in figure 15. The variation of $k_z V_{\boldsymbol{u}}$ with Ma_b is strongly analogous to $k_z^2 R_{max}$ (see figure 11*d*). Both the inner and outer peaks are present in the curves of different Ma_b. Furthermore, the $\lambda_{z,o}^+$ of $V_{\boldsymbol{u}}$ is nearly unchanged corresponding to $\lambda_{z,o} = 3.6h$, while $\lambda_{z,i}^+$ increases continuously with Ma_b, as already described in figure 12(*b*). The k^{-1} scaling in the mid-k_z range gradually deviates at high Ma_b, and the relative importance of the inner peak is enhanced in amplifying the response. In comparison, $V_{\rho T}$ experiences a much stronger variation with Ma_b than $V_{\boldsymbol{u}}$. As Ma_b increases, $k_z^+ V_{\rho T}^+$ in the large-scale region tends to diminish, while that in the small-scale region increases dramatically. Consequently, for the case $Ma_b > 0.5$, $k_z^+ V_{\rho T}^+$ starts to monotonically increase with the rise of k_z^+. It is also observed that both $V_{\boldsymbol{u}}$ and $V_{\rho T}$ are subject to the k^{-1} scaling when $Ma_b = 0.1$ in the mid-k_z range (approximately k_z^+ from 0.002 to 0.1), as labelled by the horizontal dashed lines in figure 15. With the increase of Ma_b, this scaling gradually deviates, especially for $V_{\rho T}$. In short, the motion due to the kinematic part of the forcing is much less sensitive to the compressibility effect
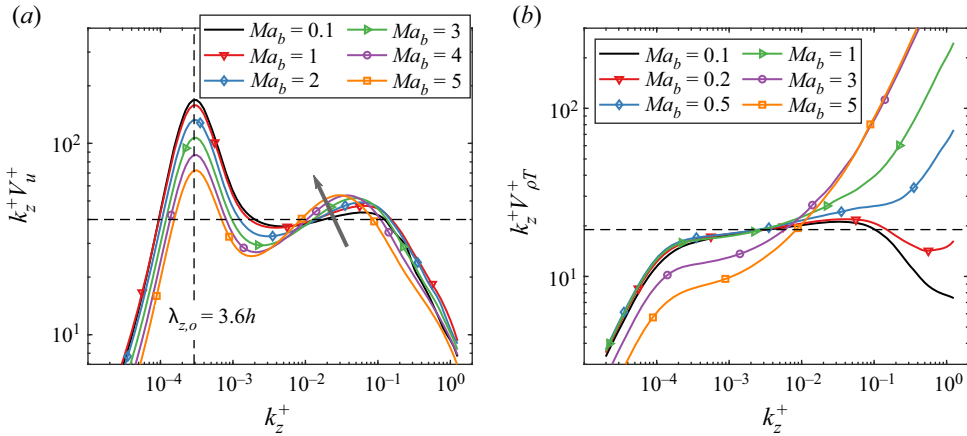
962 A7-26

Figure 15. Pre-multiplied variances of the stochastic responses to the forcing of only the (*a*) velocity components and (*b*) thermodynamic components in the cases of varying Ma_b ($Re_\tau = 6000$).

than the thermodynamic part. With Ma_b increasing, the thermodynamic components begin to dominate the total variance of the stochastic response in the small-scale region (roughly $\lambda_z^+ < 60$).

As discussed in §4.1, the response corresponding to $V_{\rho T}$ is much less coherent. Therefore, for the response to full forcing (V), the increase of $V_{\rho T}$ with Ma_b can decrease the dominance of the principal mode pair and thus the coherence of the flow. This is examined by plotting the ratio $r_V = (\theta_1 + \theta_2)/V$ for the cases of different Ma_b, as displayed in figure 16. The ratio corresponding to the optimal harmonic response, $r_\sigma = (\sigma_1^2 + \sigma_2^2)/\sum \sigma_j^2$, is also plotted. As can be seen, r_V and r_σ are not affected by Ma_b in the large-scale region near the outer peak. The motion there, with r_V and r_σ both larger than 80 %, is dominated by that induced by the kinematic part of the forcing, also insensitive to Ma_b and Re_τ (see figure 11). In the small-scale region, r_V experiences different trends of variation with Ma_b in the ranges larger and smaller than $\lambda_z^+ = 90$, respectively. It is the same for r_σ except that the dividing line is at $\lambda_z^+ = 130$. Specifically, r_V (also r_σ) increases with Ma_b for $\lambda_z^+ > 90$, i.e. the principal mode pair has an increasingly large contribution to the total energy growth, which is attributed to the increase of V_u^+. The DNS results also indicate that wall cooling tends to increase the coherence of the near-wall motion in this wavelength range. The interpretation is that the anisotropic motion is suppressed by wall cooling due to the reduction in energy exchange (Coleman *et al.* 1995; Morinishi *et al.* 2004; Duan *et al.* 2010; Zhang *et al.* 2022). In contrast, it is observed here that r_V (also r_σ) quickly decreases with Ma_b at $\lambda_z^+ < 90$, indicating a reduction in coherence and also the dominance of the principal mode pair for the total energy growth. This trend is obviously due to the enhancement of the response induced by the thermodynamic part of the forcing, as shown in figure 15(*b*).

5. Theoretical analysis of the linear operator

It is observed in figures 11(*c*) and 15 that the pre-multiplied energy amplification of the optimal harmonic and stochastic response gradually deviates from the k_z^{-2} and k_z^{-1} scalings in the mid-k_z range at higher Ma_b. We appeal to a theoretical analysis on (3.1) to support this observation.
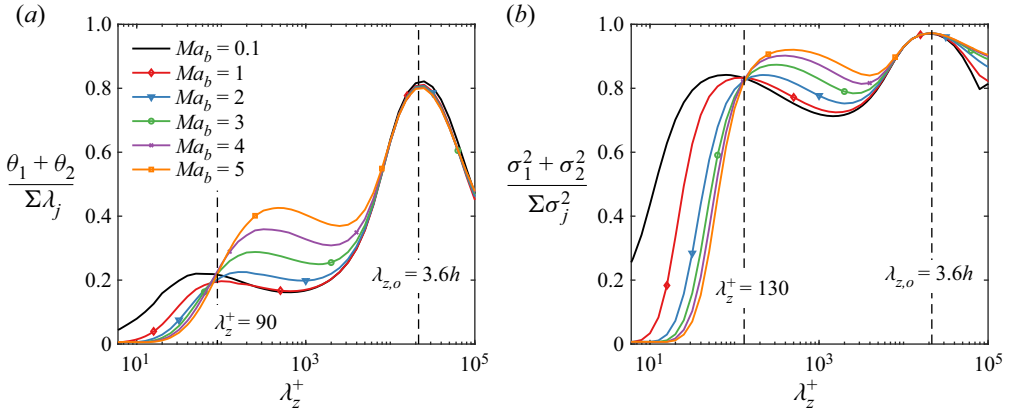
Figure 16. Contribution from the principal mode pair to the total energy amplification (in %) for the (*a*) stochastic and (*b*) optimal harmonic responses in the cases of varying Ma_b.

To simplify the form of the equations, the power law $\mu = T^n$ is adopted temporarily for derivation use instead of the original Sutherland's law. This results in only a minor difference because μ is much smaller than μ_t. The mode of $k_x = 0$ is considered, and the terms related directly to $\bar{\rho}$ and $\bar{T}$ are combined to cluster the effect of compressibility in the equation. For example, the continuity and streamwise momentum equations are written as

$$
\left.
\begin{aligned}
&\frac{\partial}{\partial t} \frac{\hat{\rho}}{\bar{\rho}} - \frac{\bar{T}_y}{\bar{T}}\,\hat{v} + \left(\hat{v}_y + \mathrm{i}k_z\hat{w}\right) = \frac{\hat{f}_\rho}{\bar{\rho}}, \\
&\frac{\partial \hat{u}}{\partial t} + \bar{U}_y\hat{v} - \frac{1}{Re_b}\left[\frac{\tilde{\mu}_{t,y}}{\bar{\rho}}\,\hat{u}_y + \frac{\tilde{\mu}_t}{\bar{\rho}}\left(\hat{u}_{yy} - k_z^2\hat{u}\right)\right] \\
&\quad - \frac{n}{Re_b}\frac{\bar{\mu}}{\bar{\rho}}\left[\left(\bar{U}_{yy} + (n-1)\bar{U}_y\frac{\bar{T}_y}{\bar{T}}\right)\frac{\hat{T}}{\bar{T}} + \bar{U}_y\frac{\hat{T}_y}{\bar{T}}\right] = \hat{f}_u,
\end{aligned}
\right\}
\tag{5.1}
$$

where the subscript y denotes the wall-normal derivative, and $\tilde{\mu}_t = \mu_t + \bar{\mu}$ is the total viscosity. As can be seen, the mean-flow coefficients are $\bar{U}$, $\bar{T}$, $\tilde{\mu}_t$, $\bar{\mu}$ and their wall-normal derivatives. The other three equations can be rearranged in the same way; their expressions are specified in Appendix C. Therefore, if the basic variable $\hat{q}$ is replaced by $\hat{q}_0$, then the operator form of the equation is

$$
\frac{\partial \hat{q}_0}{\partial t} = \mathcal{L}\hat{q}_0 + \hat{f}_0, \quad \hat{q}_0 = \left[\frac{\hat{\rho}}{\bar{\rho}},\, \hat{u},\, \hat{v},\, \hat{w},\, \frac{\hat{T}}{\bar{T}}\right],
\tag{5.2a,b}
$$

and the linear operator is

$$
\mathcal{L} = \mathcal{L}\left(\bar{U}_y,\, \bar{U}_{yy},\, \frac{\bar{T}_y}{\bar{T}},\, \frac{\bar{T}_{yy}}{\bar{T}},\, \frac{\bar{T}}{Ma_b^2},\, \frac{\tilde{\mu}_t}{\bar{\rho}},\, \frac{\tilde{\mu}_{t,y}}{\bar{\rho}},\, \frac{\bar{\mu}}{\bar{\rho}}\right).
\tag{5.3}
$$

The variation of these mean-flow coefficients reflects the influencing path of compressibility on the response behaviours. Note that κ_t and $\bar{\kappa}$ are related to viscosity through the constants Pr and Pr_t, so they are not included explicitly in the bracket. In the following, the behaviours of these mean-flow coefficients are analysed for the cases of different k_z.

962 A7-28

The self-similarity of the shape function is in terms of the normalized coordinate y^+/λ_z^+, so a rescaled coordinate is introduced as $\check{y} = \bar{k}_z(y+1)$, where $\bar{k}_z = k_z/\check{k}_z$, and $\check{k}_z$ is an arbitrarily selected reference value. Note that the overhead check in this section represents the rescaled variable, different from that defined in § 3.2 for a shape function The rescaled form of (5.2a,b) is written as

$$\frac{\partial \hat{q}_0}{\partial \check{t}} = \tilde{\mathcal{L}}\hat{q}_0 + \frac{1}{\bar{k}_z}\hat{f}_0, \tag{5.4}$$

where $\check{t} = \bar{k}_z t$. If the rescaled operator $\tilde{\mathcal{L}}$ is independent of $\bar{k}_z$, i.e. $\tilde{\mathcal{L}} = \check{\mathcal{L}}$, then Hwang & Cossu (2010b) proved that there are a k_z^{-2} scaling for R_{max} and a k_z^{-1} scaling for V in the mid-k_z range (see figure 5). Conversely, the variable that cannot be made independent of $\bar{k}_z$ is responsible for the failure of the scaling.

As $\hat{q}_0$ is a solution defined on the $\check{y}$-coordinate, its wall-normal derivative follows

$$\frac{\partial}{\partial y} = \bar{k}_z \frac{\partial}{\partial \check{y}}. \tag{5.5}$$

However, this chain rule is not applicable for the derivatives of mean-flow quantities because they are solutions on the y-coordinate. Taking the streamwise momentum equation as an example, the rescaled form is written as

$$\left. \begin{aligned} &\frac{\partial \hat{u}}{\partial \check{t}} + \frac{\bar{U}_y}{\bar{k}_z}\hat{v} - \frac{1}{Re_b}\left[\frac{\tilde{\mu}_{t,y}}{\bar{\rho}}\hat{u}_y + \frac{\bar{k}_z\tilde{\mu}_t}{\bar{\rho}}\left(\hat{u}_{\check{y}\check{y}} - \check{k}_z^2\hat{u}\right)\right] \\ &- \frac{n}{Re_b}\frac{\bar{k}_z\bar{\mu}}{\bar{\rho}}\left[\left(\frac{\bar{U}_{yy}}{\bar{k}_z^2} + (n-1)\frac{\bar{U}_y}{\bar{k}_z}\frac{\bar{T}_y}{\bar{k}_z\bar{T}}\right)\frac{\hat{T}}{\bar{T}} + \frac{\bar{U}_y}{\bar{k}_z}\frac{\hat{T}_{\check{y}}}{\bar{T}}\right] = \frac{\hat{f}_u}{\bar{k}_z}. \end{aligned} \right\} \tag{5.6}$$

The mean-flow coefficients are analysed as follows. The peaks of the perturbation in figure 9 are within the logarithmic region, where the streamwise velocity from the current velocity transformation (see (A2b)) satisfies

$$\bar{\mu}\frac{\partial \bar{U}^+}{\partial y^+} = \frac{\mathrm{d}\bar{U}_{TL}^+}{\mathrm{d}y^*} = \frac{1}{\kappa_c y^*} \quad \rightarrow \quad \bar{U}_y = \frac{u_\tau}{\kappa_c}\frac{\sqrt{\bar{T}}}{y+1}, \tag{5.7}$$

where κ_c is the Kármán constant. Therefore, the rescaled velocity gradient is

$$\frac{\bar{U}_y(y)}{\bar{k}_z} = \frac{u_\tau}{\kappa_c}\frac{\sqrt{\bar{T}(y)}}{\check{y}} = \check{U}_{\check{y}}\frac{\sqrt{\bar{T}(y)}}{\sqrt{\bar{T}(\check{y})}} \equiv K_1(y,\check{y})\,\check{U}_{\check{y}}. \tag{5.8}$$

As can be seen, only if $K_1 = 1$, i.e. $\bar{T}(y)$ is constant, is $\bar{U}_y/\bar{k}_z = \check{U}_{\check{y}}$ independent of $\bar{k}_z$ in the logarithmic region. Similarly, the temperature gradient from (A3) is

$$\frac{\bar{T}_y}{\bar{T}} = \frac{C_1\left[2(C_2 - C_3)\bar{U} + C_3\bar{U}_c\right]}{1 + C_1\bar{U}\left[(C_2 - C_3)\bar{U} + C_3\bar{U}_c\right]}\bar{U}_y \equiv C_T(y)\,\bar{U}_y, \tag{5.9}$$

so the rescaled temperature gradient is

$$\frac{\bar{T}_y(y)}{\bar{k}_z\bar{T}(y)} = C_T(y)\frac{\bar{U}_y(y)}{\bar{k}_z} = K_2\frac{\check{T}_{\check{y}}(\check{y})}{\check{T}(\check{y})}, \quad \text{where } K_2(y,\check{y}) = \frac{\sqrt{\bar{T}(y)}\,C_T(y)}{\sqrt{\bar{T}(\check{y})}\,C_T(\check{y})}. \tag{5.10}$$

For the eddy viscosity, (3.18) in the logarithmic region gives

$$\frac{\tilde{\mu}_t}{\bar{\rho}} = \frac{\kappa_c \, Re_\tau}{\rho_w} \sqrt{\bar{T}} \, (y+1) \left[1 - (y+1) \right], \tag{5.11}$$

so the rescaled version is

$$\frac{\bar{k}_z \, \tilde{\mu}_t(y)}{\bar{\rho}(y)} \approx \frac{\kappa_c \, Re_\tau}{\rho_w} \sqrt{\bar{T}} \, \check{y} \left(1 - \check{y} \right) = K_1 \frac{\check{\tilde{\mu}}_t(\check{y})}{\check{\bar{\rho}}(\check{y})}, \tag{5.12}$$

where the approximation is due to the assumption that $(y+1) \ll 1$ (recall that the wall is at $y = -1$). The other two mean-flow coefficients in (5.7) are rescaled as

$$\begin{rcases} \dfrac{\bar{U}_{yy}(y)}{\bar{k}_z^2} = \left(\dfrac{\bar{T}_y}{2\bar{k}_z \bar{T}} - \dfrac{1}{\bar{k}_z(y+1)} \right) \dfrac{\bar{U}_y(y)}{\bar{k}_z} = K_1 K_2 \left[\check{\bar{U}}_{\check{y}\check{y}}(\check{y}) + \left(1 - \dfrac{1}{K_2} \right) \dfrac{\check{\bar{U}}_{\check{y}}(\check{y})}{\check{y}} \right], \\[4mm] \dfrac{\tilde{\mu}_t(y)}{\bar{\rho}(y)} \approx K_1 K_2 \left[\dfrac{\check{\tilde{\mu}}_{t,\check{y}}(\check{y})}{\check{\bar{\rho}}} + \left(1 - \dfrac{1}{K_2} \right) \dfrac{\check{\tilde{\mu}}_t(\check{y})}{\check{y} \, \check{\bar{\rho}}(\check{y})} \right]. \end{rcases} \tag{5.13}$$

Therefore, if $K_1 = K_2 = 1$, then $\bar{U}_{yy}/\bar{k}_z^2$ and $\tilde{\mu}_t/\bar{\rho}$ are independent of $\bar{k}_z$. The rescaled expressions in (5.8), (5.10), (5.12) and (5.13) are all explicitly irrelevant of $\bar{k}_z$, and dependent on K_1 and K_2 instead. The remaining mean-flow coefficient in (5.7), $\bar{k}_z \bar{\mu}/\bar{\rho}$, is related only to $\bar{T}$ and cannot be effectively made independent of $\bar{k}_z$. The other four equations can be analysed similarly. As a result, all the mean-flow coefficients can be categorized into two groups: (i) the ones that can be rescaled using K_1 and K_2 in the logarithmic region, including $\bar{U}_y$, $\bar{U}_{yy}$, $\bar{T}_y/\bar{T}$, $\tilde{\mu}_t/\bar{\rho}$ and $\tilde{\mu}_{t,y}/\bar{\rho}$ (see (5.3)); (ii) the ones related only to $\bar{T}$ that cannot be made explicitly irrelevant to $\bar{k}_z$, including $\bar{\mu}/\bar{\rho}$ and $\bar{T}/Ma_b^2$.

In summary, three factors are primarily responsible for the potential failure of the k_z^{-2} and k_z^{-1} scalings. The first is related to the logarithmic region. If a large portion of the shape function is out of the logarithmic region, then (5.7) and equations following all fail. This is why the scaling applies only in the mid-λ_z range and is consistent with the assumption of the AEM. The second factor is the substantial variations of K_1 and K_2 at different wall-normal heights. The third factor is the enormous contribution from the terms related to $\bar{\mu}/\bar{\rho}$ and $\bar{T}/Ma_b^2$. The latter two are absent in the incompressible case, both related directly to the distribution of mean temperature.

To see the variations of K_1 and K_2, the distributions of the functions $\sqrt{\bar{T}}$ and $\sqrt{\bar{T}} \, C_T$ (see (5.8) and (5.10)) are plotted in figure 17 for the cases of different Ma_b and $Re_\tau = 6000$. As can be seen, with the rise of Ma_b, the two functions, and thus K_1 and K_2 at fixed y and $\check{y}$, experience much larger variations. Meanwhile, the other coefficients related to $\bar{T}$ also change rapidly with y^+. This explains the trend observed in figures 11(*c*) and 15 that the k^{-2} and k^{-1} scaling for R_{max} and V have larger deviations at higher Ma_b. In short, for the high-Ma_b case of the channel flow, the sizeable mean temperature gradient near the wall destroys the k_z power scaling of the response in the mid-λ_z range.

The above analysis should also have implications for the geometrical self-similarity of the response as discussed before. For example, $\sqrt{\bar{T}}$ and $\sqrt{\bar{T}} \, C_T$ in figure 17 change
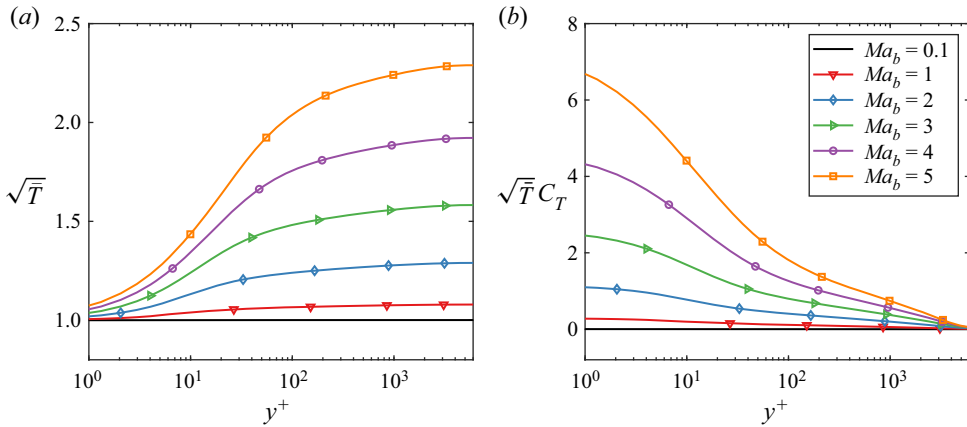
962 A7-30

(a)

(b)

Figure 17. Wall-normal distributions of the two mean-flow-related coefficients corresponding to (a) K_1 and (b) K_2, for the cases of different Ma_b ($Re_\tau = 6000$).

more slowly in the logarithmic region, especially for the former, which benefits the self-similarity of shape functions. However, the operation of the matrix inversion in (3.9a,b) obscures further analytical derivation on the perturbation equations and the transfer matrix. In fact, the results in figure 14 indicate the insensitivity of the self-similarity of the energy norm to Ma_b.

6. Summary

In this work, the linear responses of turbulent mean flow to both harmonic and stochastic forcing are investigated for supersonic channel flow. Well-established universal relations are utilized to obtain efficiently the mean profiles with a large parameter space, with Ma_b up to 5 and Re_τ up to 10^4. As a result, a systematic parameter study is feasible. Comparisons with the DNS data demonstrate the reliability of the present solver in both calculating the mean flow and serving as the base flow for the linear response analysis.

Both the optimal harmonic and stochastic forcing are considered. The response of $k_x = 0$ has the largest R_{max} and V. The pre-multiplied energy growth $k_z^2 R_{max}$ exhibits the classic bi-modal structure in terms of k_z. The two peaks correspond to the large-scale motion in the outer layer, and the near-wall small-scale motion in the buffer layer, respectively. For $k_z V$, however, the inner peak disappears when $Ma_b > 0.5$; $k_z V$ increases monotonically with k_z. A further decomposition of the forcing shows that $k_z V_u$, resulting from the kinematic part of the forcing, is quite similar to the incompressible counterpart, exhibiting the inner peak. However, the thermodynamic part, $k_z V_{\rho T}$, increases quickly at a larger k_z, and the resulting motions are much less coherent than the former. Specifically, the contribution of the most energetic mode of $V_{\rho T}$ to the energy growth is less than 3 % at $\lambda_z^+ < 100$ ($Ma_b = 2$).

The spanwise wavenumber of the outer peak is $\lambda_{z,o} \approx 3.6h$, nearly unchanged at different Ma_b and Re_τ. The motion takes the form that the input is the streamwise vortex, and the output is the streamwise streak of velocity and temperature. The temperature streak penetrates deeper towards the wall than the streamwise velocity. The spanwise wavenumber of the inner peak $\lambda_{z,i}^+$ is nearly independent of Re_τ, but increases quickly with Ma_b, due mainly to the wall-cooling effects in terms of the smaller ratio $T_w/\bar{T}_c$. From $Ma_b = 0.1$ to 5, $\lambda_{z,i}^+$ is lifted by over three times. If using semi-local units, $\lambda_{z,i}^*$ is approximately unchanged with Ma_b. Wall-cooling effects enhance

962 A7-31

the coherence of the flow for the stochastic response of $\lambda_{z,m}^+ > 90$ and the optimal harmonic response of $\lambda_{z,m}^+ > 130$, consistent with the DNS data. On the contrary, it is found that the coherence of the response with $\lambda_z^+ < \lambda_{z,m}^+$ decreases with Ma_b. This is due to the strengthening of the less-coherent motion related to $V_{\rho T}$. As a result, the cospectrum of $\langle \hat{\rho}\hat{T}^\dagger \rangle$ has a hot zone attached to the wall within the viscous layer.

The response modes with λ_z between the inner and outer peaks exhibit a geometrical self-similarity to a first approximation, with Ma_b from 0.1 to 5. The normalized energy norm is approximately collapsed using the wall-normal coordinate y^+/λ_z^+. The self-similarity is related to the logarithmic region, relatively insensitive to Ma_b and thus the compressibility effects. Finally, a theoretical analysis is conducted on the perturbation equations. The behaviour of the mean-flow coefficients is analysed within the logarithmic region. More importantly, two crucial parameters are summarized related to the dependence of the linear operator on k_z. The two parameters are related directly to the mean temperature, experiencing stronger variations in the wall-normal direction with Ma_b increase, which explains the trend that the k_z^{-2} and k_z^{-1} scalings of R_{max} and V in the mid-k_z range have increasingly large deviations with Ma_b rise.

Compared with the DNS data, the present results are more qualitative than quantitative. Some interpretations of the differences have been provided earlier in the text. Future attention will be paid to the improvement of the modelling of nonlinear forcing term, and the development of a prediction model on the energy spectra and space–time properties of the fluctuations.

Author ORCIDs.

Xianliang Chen https://orcid.org/0000-0002-7540-3395;

Cheng Cheng https://orcid.org/0000-0002-7961-793X;

Lin Fu https://orcid.org/0000-0001-8979-8415;

Jianping Gan https://orcid.org/0000-0001-9827-7929.

Appendix A. Fitting parameters and the ODE mean-flow solver

This appendix provides the details of fitting (2.7) and calculating the turbulent mean flow. For the fitting of the incompressible velocity profile, the DNS database is from Lee & Moser (2015) (downloaded at https://turbulence.oden.utexas.edu) with Re_τ from 180 to 5200. The κ_c and A_{v_t} values are looped to minimize the global relative error $\epsilon(\bar{U})$

Re_τ	$\kappa_{c,opt}$	$A_{v_t,opt}$	$\epsilon_{sgl}(\bar{U})$	$\epsilon_{glb}(\bar{U})$
182	0.550	39.8	0.56 %	1.49 %
543	0.435	26.8	0.40 %	0.82 %
1000	0.426	26.1	0.26 %	0.35 %
1995	0.422	26.2	0.14 %	0.46 %
5186	0.437	29.3	0.12 %	0.38 %
All five	0.418	25.1	—	0.70 %

Table 1. Optimal fitting parameters for (2.7) and the relative error of the turbulent mean streamwise velocity for the incompressible channel flow.

defined as

$$\epsilon(\bar{U}) = \frac{\displaystyle\int_{-1}^{0} |\bar{U}_{fit} - \bar{U}_{DNS}| \, \mathrm{d}y}{\displaystyle\int_{-1}^{0} \bar{U}_{DNS} \, \mathrm{d}y}. \tag{A1}$$

The results, with three significant digits, are given in table 1. Here, ϵ_{sgl} is the locally optimal error considering only a single profile, and ϵ_{glb} is the error using $\kappa_c = 0.418$ and $A_{v_t} = 25.1$, which are optimized considering all five profiles with equal weights. Furthermore, a trend is observed that (2.7) predicts better the mean profile at a higher Re_τ.

The compressible turbulent mean flow can be obtained through an iterative method (Griffin *et al.* 2022; Song, Zhang & Xia 2023). Here, we use four universal relations to derive an ODE for the mean flow, as summarized in §2.2. In addition to (2.7), the other three relations are specified below.

(i) The total-stress-based transformation proposed by Griffin *et al.* (2021*b*) well collapses nearly all the available profiles in the ranges $Re_\tau^* \in [200, 4000]$ and $Ma \in [0, 15]$. The expression is written as

$$\frac{\partial \bar{U}_{GFM}^+}{\partial y^*} = \frac{1}{\bar{\mu}^+} \frac{\partial \bar{U}^+}{\partial y^*} \bigg/ \left(1 + \frac{1}{\bar{\mu}^+} \frac{\partial \bar{U}^+}{\partial y^*} - \bar{\mu}^+ \frac{\partial \bar{U}^+}{\partial y^*}\right). \tag{A2a}$$

Also, the transformation proposed by Trettel & Larsson (2016) is proven to have good performance in channel flows, written as

$$\frac{\partial \bar{U}_{TL}^+}{\partial y^*} = \bar{\mu}^+ \frac{\partial \bar{U}^+}{\partial y^+}. \tag{A2b}$$

The transformed velocities $\bar{U}_{GFM}^+(y^*)$ and $\bar{U}_{TL}^+(y^*)$ are expected to match $\bar{U}_{inc}^+$ in (2.7). Note that the transformation is designed for the flow within and below the logarithmic layer, and hence may deviate in the outer region. This will be checked later through the comparison with the DNS data.

(ii) For the temperature profile, Duan & Martín (2011) summarized the DNS data from low- to high-enthalpy flows, and provided the following improved relation for a calorically

perfect gas:

$$\frac{\bar{T}}{T_\delta} = \frac{T_w}{T_\delta} + \frac{T_{aw} - T_w}{T_\delta} f_u \left(\frac{\bar{U}}{U_\delta} \right) + \frac{T_\delta - T_{aw}}{T_\delta} \left(\frac{\bar{U}}{U_\delta} \right)^2, \left.\begin{array}{c} \\ \\ \end{array}\right\}$$
$$f_u(x) = (1 - C_T)x^2 + C_T x, \quad C_T = 0.8259,$$
(A3)

where T_δ and U_δ are the boundary-layer edge values, and $T_{aw} = T_\delta[1 + r_c(\gamma - 1)/2\,Ma_\delta^2]$ is the adiabatic wall temperature with $r_c = 0.9$ as the recovery factor. The original data are based on the Favre average, while the Reynolds-averaged quantity is used here. The difference between the two averages is generally small at moderate Ma (Huang *et al.* 1995), and the accuracy will be examined later. Equation (A3) also works for channel flows, where T_δ, U_δ and Ma_δ are replaced by $\bar{T}_c$, $\bar{U}_c$ and Ma_c.

(iii) In terms of the outer boundary condition, Song *et al.* (2022) proposed an empirical scaling to connect $\bar{T}_c$ and $\bar{U}_c$:

$$\frac{\bar{T}_c}{T_w} = 1 + C_{Pr} \frac{\bar{U}_c}{U_b} \frac{\gamma - 1}{2} Ma_b^2, \quad C_{Pr} = 1.034 Pr.$$
(A4a,b)

Most of the relative errors of computed $\bar{T}_c$ were shown to be below 1.5 % for the cases with Re_b and Ma_b ranging from 3000 to 34 000 and 0.5 to 4.0, respectively.

Based on (A2b), the equation to be solved is

$$\frac{\bar{\mu}}{u_\tau} \frac{\partial \bar{U}}{\partial y^+} = \frac{\partial \bar{U}_{TL}^+}{\partial y^*} = \frac{\mathrm{d}\bar{U}_{inc}^+(y^*; Re_\tau^*)}{\mathrm{d}y^*}.$$
(A5)

Here, u_τ is also an unknown. The version using (A2a) can be derived similarly. The combination of (A3) and (A4a,b) results in the following quadratic relation between $\bar{T}$ and $\bar{U}$:

$$\frac{\bar{T}}{T_w} = 1 + C_1 \frac{\bar{U}}{U_b} \left[(C_2 - C_3) \frac{\bar{U}}{U_b} + C_3 \frac{\bar{U}_c}{U_b} \right], \quad \left\{\begin{array}{l} C_1 = \dfrac{\gamma - 1}{2} Ma_b^2, \\[2mm] C_2 = C_{Pr} \dfrac{U_b}{\bar{U}_c}, \\[2mm] C_3 = C_T (C_2 + r_c). \end{array}\right.$$
(A6a,b)

Note that $U_b = T_w = 1$ under the current definition of non-dimensional quantities (see (2.2)). The pressure is assumed to be a constant along the wall-normal direction, so the mean density is expressed as $\bar{\rho} = \rho_w T_w / \bar{T}$. The two unknowns u_τ and ρ_w are solved using the two constraints in (2.4). Therefore, the ODE set is

$$F_1(\bar{U}, u_\tau) = \bar{\mu} \frac{\partial \bar{U}}{\partial y^+} - u_\tau \frac{\mathrm{d}\bar{U}_{inc}^+(y^*; Re_\tau^*)}{\mathrm{d}y^*} = 0, \left.\begin{array}{c} \\ \\ \\ \end{array}\right\}$$
$$F_2(\bar{U}) = \int_{-1}^{0} \frac{\bar{U} - 1}{\bar{T}} \mathrm{d}y = 0.$$
(A7)

The only boundary condition required is $\bar{U}|_w = 0$. For numerical solutions, the Chebyshev collocation method is adopted to cope with the derivatives and integrals. The computational domain is $y \in [-1, 0]$, and the grid number is $N_y = 301$. The initial

No.	Re_τ^*	Ma_b	Re_τ	Re_b	$\epsilon(\bar{U})$	$\epsilon(\bar{T})$	$\epsilon(\bar{\rho})$	Source
(1)	202.8	4.0	1017.5	10 000	1.98 %	3.92 %	3.97 %	TL
(2)	208.4	3.0	649.9	7500	1.72 %	2.78 %	2.84 %	TL
(3)	334.8	1.5	499.6	7667	1.02 %	1.28 %	0.80 %	MP
(4)	337.1	1.5	505.9	7667	1.07 %	0.37 %	0.13 %	YH
(5)	395.5	3.0	1232.5	15 000	1.22 %	1.15 %	1.23 %	TL
(6)	396.4	0.7	437.4	7500	0.67 %	0.04 %	0.02 %	TL
(7)	396.5	0.8	452.1	7667	0.76 %	0.11 %	0.07 %	YH
(8)	406.3	1.7	663.1	10 000	1.13 %	0.32 %	0.34 %	TL
(9)	591.1	0.7	652.1	11 750	0.74 %	0.05 %	0.06 %	TL
(10)	595.8	1.7	971.7	15 500	0.61 %	0.15 %	0.11 %	TL
(11)	600.7	3.0	1876.1	24 000	0.75 %	0.40 %	0.48 %	TL
(12)	679.6	1.5	1010.9	17 000	0.44 %	1.01 %	0.57 %	MP
(13)	682.8	1.5	1027.3	17 000	1.05 %	0.35 %	0.77 %	YH
(14)	797.5	0.8	909.0	17 000	0.84 %	0.03 %	0.18 %	YH
(15)	1265.8	1.5	1911.0	34 000	1.42 %	0.93 %	1.32 %	YH
(16)	1482.7	0.8	1690.2	34 000	0.71 %	0.15 %	0.29 %	YH

Table 2. Case parameters and the relative errors between the mean profiles from the ODE solver and the published DNS data. The abbreviations for the data source are TL from Trettel & Larsson (2016), MP from Modesti & Pirozzoli (2016), and YH from Yao & Hussain (2020).

$\bar{U}$ for iteration uses the incompressible profile. Newton's iteration is adopted for quick convergence.

For verification, the results from the present ODE solver are compared with the published DNS data. The cases with $Re_\tau^* > 200$ are selected and the results are summarized in table 2. The relative errors of $\bar{T}$ and $\bar{\rho}$ are defined similarly to (A1). As can be seen, for the fourteen cases with $Re_\tau^* > 300$, $\epsilon(\bar{U})$, $\epsilon(\bar{T})$ and $\epsilon(\bar{\rho})$ are all smaller than 1.5 %, and the average error is only 0.60 %, which demonstrates the reliability of the present ODE solver. If (A2b) is replaced by (A2a), then the average error is generally 1.5 % larger, and is located mainly in the outer region. It is noted that both (A2a) and (A2b) are not specially designed for the flow in the outer region, but (A2b) has unexpected good performance there and is thus used for later calculations.

Figure 18 gives the comparison of the mean profiles for two representative cases with moderate errors, i.e. nos. (11) and (16). The excellent agreement between those from the ODE solver and the DNS data has already been shown in table 2. A visible difference in the velocity profile is near the junction of the buffer and logarithm layer, which originates from the incompressible curve fit of (2.7) and diminishes with the rise of Re_τ. The differences in the density and temperature profiles are mainly because of the slight difference in $\bar{T}_c$ and a slightly varying pressure along the wall-normal direction.

Appendix B. Verification of the response solver

The present linear response solver is verified through comparison with published results. The first case is from Moarref *et al.* (2013) for an incompressible turbulent channel flow with $Re_\tau = 2003$. Figure 19 provides the comparison of the first twenty singular values of the transfer matrix H (see (3.9a,b)) for the harmonic response of $\lambda_x^+ = 700$, $\lambda_z^+ = 100$ and $\omega/k_x = 10$. As can be seen, excellent agreement is obtained. The second case is from Hwang & Cossu (2010b) for an incompressible turbulent channel flow with $Re_\tau = 10^4$. The pre-multiplied energy amplification of the stochastic response is calculated for the
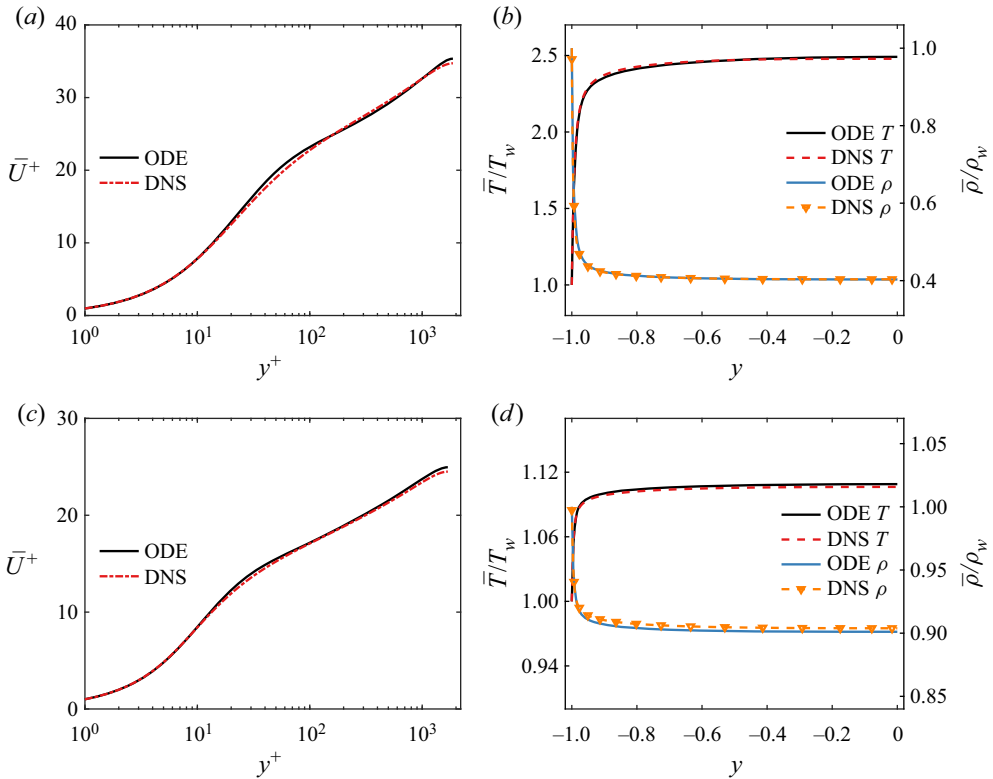
Figure 18. Mean profiles of the (a,c) streamwise velocity and (b,d) temperature for cases (a,b) no. (11) from Trettel & Larsson (2016), and (c,d) no. (16) from Yao & Hussain (2020), as in table 2.

mode of various k_x and k_z. The agreement with the published results is good as well. Note that figure 19(b) is the incompressible counterpart to the results in figures 5 and 15. The third case is from Dawson & McKeon (2020) for a compressible flat-plate turbulent boundary layer with $Ma_\infty = 2$ and $Re_\tau = 900$, with the mean flow from Pirozzoli & Bernardini (2011). The component shape functions of the optimal response mode ($k_x \delta_{99} = \pi/2$, $k_z \delta_{99} = 2\pi$ and $\omega/k_x = 0.8U_\infty$, with δ_{99} the nominal thickness) are demonstrated in figure 19(c), which is again in close agreement with the reference data. The above comparisons demonstrate the reliability of the present solver in calculating the linear responses to both harmonic and stochastic forcing.

Appendix C. Matrix coefficients and the perturbation equation

Non-zero elements of the matrix coefficients in (3.1) are listed below. Note that $\tilde{\mu}_t = \mu_t + \bar{\mu}$ and $\tilde{\kappa}_t = \kappa_t + \bar{\kappa}$, and the subscripts y and T denote the corresponding partial derivatives.

Matrix F:

$$\boldsymbol{F}_{1,1} = 1, \quad \boldsymbol{F}_{2,2} = \bar{\rho}, \quad \boldsymbol{F}_{3,3} = \bar{\rho}, \quad \boldsymbol{F}_{4,4} = \bar{\rho}, \quad \boldsymbol{F}_{5,5} = \bar{\rho}c_v, \quad \boldsymbol{F}_{5,1} = -Ec\,R\bar{T}.$$
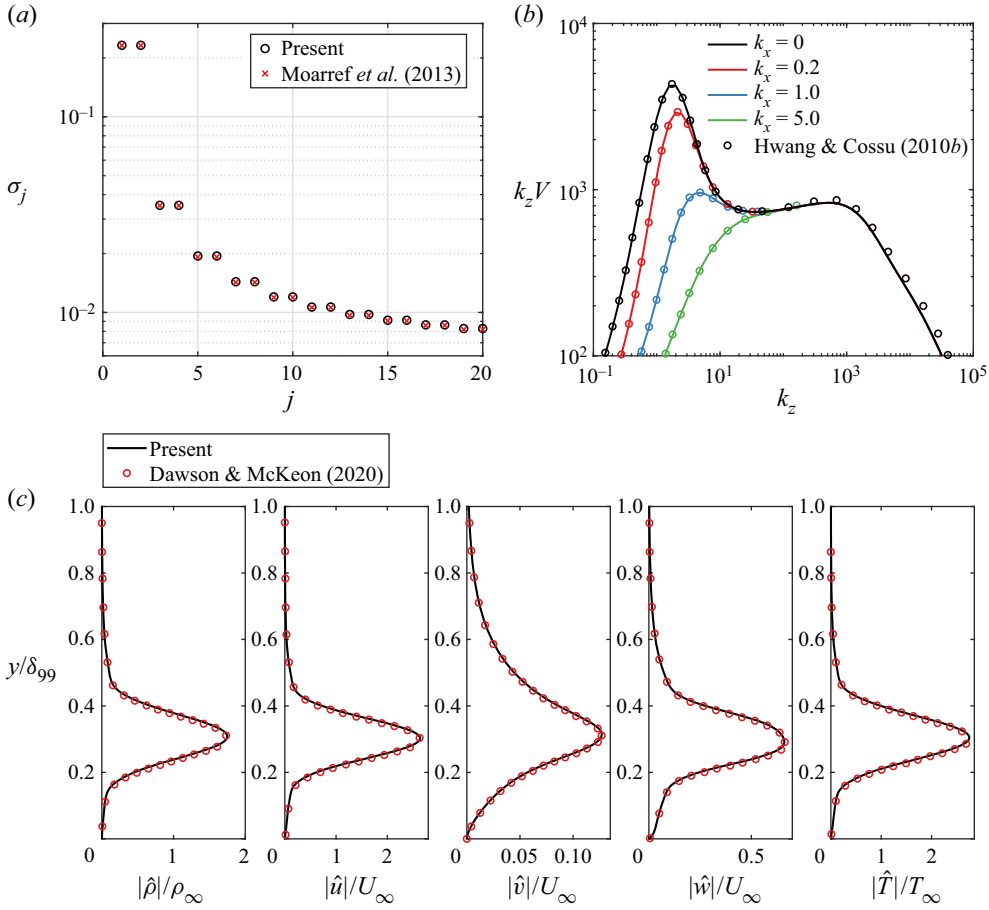$$(C1a\text{–}f)$$

Figure 19. (*a*) The first 20 singular values of the transfer matrix for the harmonic response and (*b*) the pre-multiplied energy amplification of the stochastic response of various k_x and k_z for the incompressible turbulent channel flow cases. (*c*) The shape functions of the optimal response mode for the compressible turbulent boundary layer case. The reference data are from Moarref *et al.* (2013), Hwang & Cossu (2010*b*) and Dawson & McKeon (2020), respectively.

Matrix A:

$$
\left.
\begin{aligned}
& A_{1,1} = \bar{U}, \quad A_{1,2} = \bar{\rho}, \quad A_{2,1} = R\bar{T}, \quad A_{2,2} = \bar{\rho}\bar{U}, \quad A_{2,3} = -\frac{\tilde{\mu}_{t,y}}{Re_b}, \\
& A_{2,5} = \bar{\rho}R, \quad A_{3,2} = \frac{2}{3}\frac{\tilde{\mu}_{t,y}}{Re_b}, \quad A_{3,3} = \bar{\rho}\bar{U}, \quad A_{3,5} = -\frac{\bar{\mu}_T \bar{U}_y}{Re_b}, \\
& A_{4,4} = \bar{\rho}\bar{U}, \quad A_{5,1} = -Ec\,R\bar{T}\bar{U}, \quad A_{5,3} = -\frac{2\,Ec\,\tilde{\mu}_t \bar{U}_y}{Re_b}, \quad A_{5,5} = \bar{\rho}c_v\bar{U}.
\end{aligned}
\right\}
\quad (C2)
$$

Matrix B:

$$
\left.\begin{aligned}
&\boldsymbol{B}_{1,3} = \bar{\rho}, \quad \boldsymbol{B}_{2,2} = -\frac{\tilde{\mu}_{t,y}}{Re_b}, \quad \boldsymbol{B}_{2,5} = -\frac{\bar{\mu}_T \bar{U}_y}{Re_b}, \quad \boldsymbol{B}_{3,1} = R\bar{T}, \quad \boldsymbol{B}_{3,3} = -\frac{4}{3}\frac{\tilde{\mu}_{t,y}}{Re_b}, \\
&\boldsymbol{B}_{3,5} = \bar{\rho}R, \quad \boldsymbol{B}_{4,4} = -\frac{\tilde{\mu}_{t,y}}{Re_b}, \quad \boldsymbol{B}_{5,2} = -\frac{2\,Ec\,\tilde{\mu}_t \bar{U}_y}{Re_b}, \quad \boldsymbol{B}_{5,5} = -\frac{\tilde{\kappa}_{t,y} + \bar{\kappa}_T \bar{T}_y}{Re_b}.
\end{aligned}\right\}
$$
$$(C3)$$

Matrix C:

$$
\boldsymbol{C}_{1,4} = \bar{\rho}, \quad \boldsymbol{C}_{3,4} = \frac{2}{3}\frac{\tilde{\mu}_{t,y}}{Re_b}, \quad \boldsymbol{C}_{4,1} = R\bar{T}, \quad \boldsymbol{C}_{4,3} = -\frac{\tilde{\mu}_{t,y}}{Re_b}, \quad \boldsymbol{C}_{4,5} = \bar{\rho}R. \quad (C4a\text{–}e)
$$

Matrix D:

$$
\left.\begin{aligned}
&\boldsymbol{D}_{1,3} = \bar{\rho}_y, \quad \boldsymbol{D}_{2,3} = \bar{\rho}\bar{U}_y, \quad \boldsymbol{D}_{2,5} = -\frac{\bar{\mu}_T \bar{U}_{yy} + \bar{\mu}_{yT}\bar{U}_y}{Re_b}, \quad \boldsymbol{D}_{3,1} = R\bar{T}_y, \quad \boldsymbol{D}_{3,5} = \bar{\rho}_y R, \\
&\boldsymbol{D}_{5,3} = \bar{\rho}c_v \bar{T}_y - Ec\,\bar{T}R\bar{\rho}_y, \quad \boldsymbol{D}_{5,5} = -\frac{Ec\,\bar{\mu}_T \bar{U}_y^2 + \bar{\kappa}_{yT}\bar{T}_y + \bar{\kappa}_T \bar{T}_{yy}}{Re_b}.
\end{aligned}\right\}
$$
$$(C5)$$

Matrix H:

$$
\left.\begin{aligned}
&\boldsymbol{H}_{xx,2,2} = \frac{4}{3}\frac{\tilde{\mu}_t}{Re_b}, \quad \boldsymbol{H}_{yy,2,2} = \frac{\tilde{\mu}_t}{Re_b}, \quad \boldsymbol{H}_{zz,2,2} = \frac{\tilde{\mu}_t}{Re_b}, \\
&\boldsymbol{H}_{xy,2,3} = \frac{1}{3}\frac{\tilde{\mu}_t}{Re_b}, \quad \boldsymbol{H}_{zx,2,4} = \frac{1}{3}\frac{\tilde{\mu}_t}{Re_b}, \\
&\boldsymbol{H}_{xx,3,3} = \frac{\tilde{\mu}_t}{Re_b}, \quad \boldsymbol{H}_{yy,3,3} = \frac{4}{3}\frac{\tilde{\mu}_t}{Re_b}, \quad \boldsymbol{H}_{zz,3,3} = \frac{\tilde{\mu}_t}{Re_b}, \\
&\boldsymbol{H}_{xy,3,2} = \frac{1}{3}\frac{\tilde{\mu}_t}{Re_b}, \quad \boldsymbol{H}_{yz,3,4} = \frac{1}{3}\frac{\tilde{\mu}_t}{Re_b}, \\
&\boldsymbol{H}_{xx,4,4} = \frac{\tilde{\mu}_t}{Re_b}, \quad \boldsymbol{H}_{yy,4,4} = \frac{\tilde{\mu}_t}{Re_b}, \quad \boldsymbol{H}_{zz,4,4} = \frac{4}{3}\frac{\tilde{\mu}_t}{Re_b}, \\
&\boldsymbol{H}_{yz,4,3} = \frac{1}{3}\frac{\tilde{\mu}_t}{Re_b}, \quad \boldsymbol{H}_{zx,4,2} = \frac{1}{3}\frac{\tilde{\mu}_t}{Re_b}, \\
&\boldsymbol{H}_{xx,5,5} = \frac{\tilde{\kappa}_t}{Re_b}, \quad \boldsymbol{H}_{yy,5,5} = \frac{\tilde{\kappa}_t}{Re_b}, \quad \boldsymbol{H}_{zz,5,5} = \frac{\tilde{\kappa}_t}{Re_b}.
\end{aligned}\right\}
$$
$$(C6)$$

In addition to the two equations in (5.1), the other three perturbation equations are written as

$$
\frac{\partial \hat{v}}{\partial t} + \frac{\bar{T}}{\gamma\,Ma_b^2}\left(\frac{\bar{T}_y}{\bar{T}}\frac{\hat{\rho}}{\bar{\rho}} + \frac{\hat{\rho}_y}{\bar{\rho}} - \frac{\bar{T}_y}{\bar{T}}\frac{\hat{T}}{\bar{T}} + \frac{\hat{T}_y}{\bar{T}}\right)
$$
$$
- \frac{1}{Re_b}\left[\frac{\tilde{\mu}_{t,y}}{\bar{\rho}}\left(\frac{4}{3}\hat{v}_y - \frac{2\mathrm{i}k_z}{3}\hat{w}\right) + \frac{\tilde{\mu}_t}{\bar{\rho}}\left(\frac{4}{3}\hat{v}_{yy} - k_z^2\hat{v} + \frac{\mathrm{i}k_z}{3}\hat{w}_y\right)\right] = \hat{f}_v, \qquad (C7a)
$$

$$\frac{\partial \hat{w}}{\partial t} + \mathrm{i}k_z \frac{\bar{T}}{\gamma\, Ma_b^2} \left(\frac{\hat{\rho}}{\bar{\rho}} + \frac{\hat{T}}{\bar{T}}\right)$$

$$- \frac{1}{Re_b}\left[\frac{\tilde{\mu}_{t,y}}{\bar{\rho}}\left(\hat{w}_y + \mathrm{i}k_z \hat{v}\right) + \frac{\tilde{\mu}_t}{\bar{\rho}}\left(\hat{w}_{yy} - \frac{4}{3}k_z^2\hat{w} + \frac{\mathrm{i}k_z}{3}\hat{v}_y\right)\right] = \hat{f}_w, \qquad \text{(C7}b\text{)}$$

$$\frac{\partial}{\partial t}\frac{\hat{T}}{\bar{T}} + \frac{\bar{T}_y}{\bar{T}}\hat{v} + (\gamma - 1)\left(\hat{v}_y + \mathrm{i}k_z\hat{w}\right) - \frac{\gamma}{Re_b}\left[\frac{\kappa_{t,y}}{\bar{\rho}}\frac{\hat{T}_y}{\bar{T}} + \frac{\kappa_t}{\bar{\rho}}\left(\frac{\hat{T}_{yy}}{\bar{T}} - k_z^2\frac{\hat{T}}{\bar{T}}\right)\right]$$

$$- \frac{\gamma - 1}{Re_b}\frac{\gamma\, Ma_b^2}{\bar{T}}\bar{U}_y\left(n\bar{U}_y\frac{\bar{\mu}}{\bar{\rho}}\frac{\hat{T}}{\bar{T}} + 2\frac{\tilde{\mu}_t}{\bar{\rho}}\hat{u}_y\right)$$

$$- \frac{n\gamma}{Re_b}\frac{\bar{\kappa}}{\bar{\rho}}\left[\left(\frac{\bar{T}_{yy}}{\bar{T}} + (n-1)\left(\frac{\bar{T}_y}{\bar{T}}\right)^2\right)\frac{\hat{T}}{\bar{T}} + \frac{\bar{T}_y}{\bar{T}}\frac{\hat{T}_y}{\bar{T}}\right] = \frac{\hat{f}_T}{\bar{T}}. \qquad \text{(C7}c\text{)}$$

REFERENCES

DEL ÁLAMO, J.C. & JIMÉNEZ, J. 2003 Spectra of the very large anisotropic scales in turbulent channels. *Phys. Fluids* **15** (6), L41–L44.

DEL ÁLAMO, J.C. & JIMÉNEZ, J. 2006 Linear energy amplification in turbulent channels. *J. Fluid Mech.* **559**, 205–213.

ALIZARD, F., GIBIS, T., SELENT, B., RIST, U. & WENZEL, C. 2022 Stochastic receptivity of laminar compressible boundary layers: an input–output analysis. *Phys. Rev. Fluids* **7** (7), 073902.

ALIZARD, F., PIROZZOLI, S., BERNARDINI, M. & GRASSO, F. 2015 Optimal transient growth in compressible turbulent boundary layers. *J. Fluid Mech.* **770**, 124–155.

AMARAL, F.R., CAVALIERI, A.V.G., MARTINI, E., JORDAN, P. & TOWNE, A. 2021 Resolvent-based estimation of turbulent channel flow using wall measurements. *J. Fluid Mech.* **927**, A17.

BAE, H.J., DAWSON, S.T. & MCKEON, B.J. 2020*a* Studying the effect of wall cooling in supersonic boundary layer flow using resolvent analysis. *AIAA Scitech 2020 Forum*. AIAA.

BAE, H.J., DAWSON, S.T.M. & MCKEON, B.J. 2020*b* Resolvent-based study of compressibility effects on supersonic turbulent boundary layers. *J. Fluid Mech.* **883**, A29.

BAI, T., GRIFFIN, K.P. & FU, L. 2022 Compressible velocity transformations for various noncanonical wall-bounded turbulent flows. *AIAA J.* **60**, 4325–4337.

BAMIEH, B. & DAHLEH, M. 2001 Energy amplification in channel flows with stochastic excitation. *Phys. Fluids* **13** (11), 3258–3269.

BEWLEY, T.R. & LIU, S. 1998 Optimal and robust control and estimation of linear paths to transition. *J. Fluid Mech.* **365**, 305–349.

BUSEMANN, A. 1931 *Handbuch der experimentalphysik*, vol. 4. Geest und Port.

BUTLER, K.M. & FARRELL, B.F. 1993 Optimal perturbations and streak spacing in wall-bounded turbulent shear flow. *Phys. Fluids* A **5** (3), 774–777.

CESS, R.D. 1958 A survey of the literature on heat transfer in turbulent tube flow. *Tech. Rep.* 8-0529-R24. Westinghouse.

CHEN, X., WANG, L. & FU, S. 2022 Energy transfer of hypersonic and high-enthalpy boundary layer instabilities and transition. *Phys. Rev. Fluids* **7** (3), 033901.

CHENG, C. & FU, L. 2022*a* Consistency between the attached-eddy model and the inner–outer interaction model: a study of streamwise wall-shear stress fluctuations in a turbulent channel flow. *J. Fluid Mech.* **942**, R9.

CHENG, C. & FU, L. 2022*b* Large-scale motions and self-similar structures in compressible turbulent channel flows. *Phys. Rev. Fluids* **7**, 114604.

CHENG, C., LI, W., LOZANO-DURÁN, A. & LIU, H. 2019 Identity of attached eddies in turbulent channel flows with bidimensional empirical mode decomposition. *J. Fluid Mech.* **870**, 1037–1071.

CHENG, C., SHYY, W. & FU, L. 2022 Streamwise inclination angle of wall-attached eddies in turbulent channel flows. *J. Fluid Mech.* **946**, A49.

CHU, B.-T. 1965 On the energy transfer to small disturbances in fluid flow (part I). *Acta Mechanica* **1** (3), 215–234.

CLENSHAW, C.W. & CURTIS, A.R. 1960 A method for numerical integration on an automatic computer. *Numer. Math.* **2** (1), 197–205.

COGO, M., SALVADORE, F., PICANO, F. & BERNARDINI, M. 2022 Direct numerical simulation of supersonic and hypersonic turbulent boundary layers at moderate–high Reynolds numbers and isothermal wall condition. *J. Fluid Mech.* **945**, A30.

COLEMAN, G.N., KIM, J. & MOSER, R.D. 1995 A numerical study of turbulent supersonic isothermal-wall channel flow. *J. Fluid Mech.* **305**, 159–183.

COSSU, C., PUJALS, G. & DEPARDON, S. 2009 Optimal transient growth and very large-scale structures in turbulent boundary layers. *J. Fluid Mech.* **619**, 79–94.

CROCCO, L. 1932 Sulla trasmissione del calore da una lamina piana a un fluido scorrente ad alta velocita. *L'Aerotecnica* **12**, 181–197.

DAWSON, S.T.M. & MCKEON, B.J. 2020 Prediction of resolvent mode shapes in supersonic turbulent boundary layers. *Intl J. Heat Fluid Flow* **85**, 108677.

DI RENZO, M., FU, L. & URZAY, J. 2020 HTR solver: an open-source exascale-oriented task-based multi-GPU high-order code for hypersonic aerothermodynamics. *Comput. Phys. Commun.* **255**, 107262.

DI RENZO, M. & URZAY, J. 2021 Direct numerical simulation of a hypersonic transitional boundary layer at suborbital enthalpies. *J. Fluid Mech.* **912**, A29.

VAN DRIEST, E.R. 1951 Turbulent boundary layer in compressible fluids. *J. Aeronaut. Sci.* **18** (3), 145–160.

DUAN, L., BEEKMAN, I. & MARTIN, M.P. 2010 Direct numerical simulation of hypersonic turbulent boundary layers. Part 2. Effect of wall temperature. *J. Fluid Mech.* **655**, 419–445.

DUAN, L., BEEKMAN, I. & MARTÍN, M.P. 2011 Direct numerical simulation of hypersonic turbulent boundary layers. Part 3. Effect of Mach number. *J. Fluid Mech.* **672**, 245–267.

DUAN, L. & MARTÍN, M.P. 2011 Direct numerical simulation of hypersonic turbulent boundary layers. Part 4. Effect of high enthalpy. *J. Fluid Mech.* **684**, 25–59.

ELLINGSEN, T. & PALM, E. 1975 Stability of linear flow. *Phys. Fluids* **18** (4), 487–488.

FARRELL, B.F. & IOANNOU, P.J. 1993 Stochastic forcing of the linearized Navier–Stokes equations. *Phys. Fluids* A **5** (11), 2600–2609.

FU, L., BOSE, S. & MOIN, P. 2022 Prediction of aerothermal characteristics of a generic hypersonic inlet flow. *Theor. Comput. Fluid Dyn.* **36** (2), 345–368.

FU, L., KARP, M., BOSE, S.T., MOIN, P. & URZAY, J. 2021 Shock-induced heating and transition to turbulence in a hypersonic boundary layer. *J. Fluid Mech.* **909**, A8.

GANAPATHISUBRAMANI, B., CLEMENS, N.T. & DOLLING, D.S. 2006 Large-scale motions in a supersonic turbulent boundary layer. *J. Fluid Mech.* **556**, 271–282.

GRIFFIN, K.P., FU, L. & MOIN, P. 2021*a* The effect of compressibility on grid-point and time-step requirements for simulations of wall-bounded turbulent flows. In *Center for Turbulence Research Annual Research Briefs* (ed. P. Moin), pp. 109–117. Center for Turbulence Research.

GRIFFIN, K.P., FU, L. & MOIN, P. 2021*b* Velocity transformation for compressible wall-bounded turbulent flows with and without heat transfer. *Proc. Natl Acad. Sci. USA* **118** (34), e2111144118.

GRIFFIN, K.P., FU, L. & MOIN, P. 2022 Near-wall model for compressible turbulent boundary layers based on an inverse velocity transformation. In *Center for Turbulence Research Annual Research Briefs* (ed. P. Moin), pp. 3–12. Center for Turbulence Research.

HAMILTON, J.M., KIM, J. & WALEFFE, F. 1995 Regeneration mechanisms of near-wall turbulence structures. *J. Fluid Mech.* **287**, 317–348.

HUANG, J., DUAN, L. & CHOUDHARI, M.M. 2022 Direct numerical simulation of hypersonic turbulent boundary layers: effect of spatial evolution and Reynolds number. *J. Fluid Mech.* **937**, A3.

HUANG, P.G., COLEMAN, G.N. & BRADSHAW, P. 1995 Compressible turbulent channel flows: DNS results and modelling. *J. Fluid Mech.* **305**, 185–218.

HUTCHINS, N. & MARUSIC, I. 2007 Large-scale influences in near-wall turbulence. *Phil. Trans. R. Soc. Lond.* A **365** (1852), 647–664.

HWANG, Y. 2015 Statistical structure of self-sustaining attached eddies in turbulent channel flow. *J. Fluid Mech.* **767**, 254–289.

HWANG, Y. & COSSU, C. 2010*a* Amplification of coherent streaks in the turbulent Couette flow: an input–output analysis at low Reynolds number. *J. Fluid Mech.* **643**, 333–348.

HWANG, Y. & COSSU, C. 2010*b* Linear non-normal energy amplification of harmonic and stochastic forcing in the turbulent channel flow. *J. Fluid Mech.* **664**, 51–73.

HWANG, Y. & ECKHARDT, B. 2020 Attached eddy model revisited using a minimal quasi-linear approximation. *J. Fluid Mech.* **894**, A23.

JIMÉNEZ, J. 2013 Near-wall turbulence. *Phys. Fluids* **25** (10), 101302.

JOVANOVIĆ, M.R. 2021 From bypass transition to flow control and data-driven turbulence modeling: an input–output viewpoint. *Annu. Rev. Fluid Mech.* **53** (1), 311–345.

JOVANOVIĆ, M.R. & BAMIEH, B. 2005 Componentwise energy amplification in channel flows. *J. Fluid Mech.* **534**, 145–183.

KIM, J. & BEWLEY, T.R. 2006 A linear systems approach to flow control. *Annu. Rev. Fluid Mech.* **39** (1), 383–417.

KIM, K.C. & ADRIAN, R.J. 1999 Very large-scale motion in the outer layer. *Phys. Fluids* **11** (2), 417–422.

KLINE, S.J., REYNOLDS, W.C., SCHRAUB, F.A. & RUNSTADLER, P.W. 1967 The structure of turbulent boundary layers. *J. Fluid Mech.* **30** (4), 741–773.

LEE, M. & MOSER, R.D. 2015 Direct numerical simulation of turbulent channel flow up to $Re_\tau = 5200$. *J. Fluid Mech.* **774**, 395–415.

MADHUSUDANAN, A. & MCKEON, B.J. 2022 Stochastic forcing to a linearized Navier–Stokes based model for laminar compressible boundary layers. *AIAA Scitech 2022 Forum*.

MALKUS, W.V.R. 1956 Outline of a theory of turbulent shear flow. *J. Fluid Mech.* **1** (5), 521–539.

MARUSIC, I., MATHIS, R. & HUTCHINS, N. 2010*a* Predictive model for wall-bounded turbulent flow. *Science* **329** (5988), 193–196.

MARUSIC, I., MCKEON, B.J., MONKEWITZ, P.A., NAGIB, H.M., SMITS, A.J. & SREENIVASAN, K.R. 2010*b* Wall-bounded turbulent flows at high Reynolds numbers: recent advances and key issues. *Phys. Fluids* **22** (6), 065103.

MARUSIC, I. & MONTY, J.P. 2019 Attached eddy model of wall turbulence. *Annu. Rev. Fluid Mech.* **51** (1), 49–74.

MCKEON, B.J. 2017 The engine behind (wall) turbulence: perspectives on scale interactions. *J. Fluid Mech.* **817**, P1.

MCKEON, B.J. 2019 Self-similar hierarchies and attached eddies. *Phys. Rev. Fluids* **4** (8), 082601.

MCKEON, B.J. & SHARMA, A.S. 2010 A critical-layer framework for turbulent pipe flow. *J. Fluid Mech.* **658**, 336–382.

MCMULLEN, R.M., ROSENBERG, K. & MCKEON, B.J. 2020 Interaction of forced Orr–Sommerfeld and Squire modes in a low-order representation of turbulent channel flow. *Phys. Rev. Fluids* **5** (8), 084607.

MOARREF, R. & JOVANOVIĆ, M.R. 2012 Model-based design of transverse wall oscillations for turbulent drag reduction. *J. Fluid Mech.* **707**, 205–240.

MOARREF, R., JOVANOVIĆ, M.R., TROPP, J.A., SHARMA, A.S. & MCKEON, B.J. 2014 A low-order decomposition of turbulent channel flow via resolvent analysis and convex optimization. *Phys. Fluids* **26** (5), 051701.

MOARREF, R., SHARMA, A.S., TROPP, J.A. & MCKEON, B.J. 2013 Model-based scaling of the streamwise energy density in high-Reynolds-number turbulent channels. *J. Fluid Mech.* **734**, 275–316.

MODESTI, D. & PIROZZOLI, S. 2016 Reynolds and Mach number effects in compressible turbulent channel flow. *Intl J. Heat Fluid Flow* **59**, 33–49.

MOIN, P. & MAHESH, K. 1998 Direct numerical simulation: a tool in turbulence research. *Annu. Rev. Fluid Mech.* **30**, 539–578.

MORINISHI, Y., TAMANO, S. & NAKABAYASHI, K. 2004 Direct numerical simulation of compressible turbulent channel flow between adiabatic and isothermal walls. *J. Fluid Mech.* **502**, 273–308.

MORRA, P., NOGUEIRA, P.A.S., CAVALIERI, A.V.G. & HENNINGSON, D.S. 2021 The colour of forcing statistics in resolvent analyses of turbulent channel flows. *J. Fluid Mech.* **907**, A24.

MORRA, P., SEMERARO, O., HENNINGSON, D.S. & COSSU, C. 2019 On the relevance of Reynolds stresses in resolvent analyses of turbulent wall-bounded flows. *J. Fluid Mech.* **867**, 969–984.

NOGUEIRA, P.A.S., MORRA, P., MARTINI, E., CAVALIERI, A.V.G. & HENNINGSON, D.S. 2021 Forcing statistics in resolvent analysis: application in minimal turbulent Couette flow. *J. Fluid Mech.* **908**, A32.

PASSIATORE, D., SCIACOVELLI, L., CINNELLA, P. & PASCAZIO, G. 2022 Thermochemical non-equilibrium effects in turbulent hypersonic boundary layers. *J. Fluid Mech.* **941**, A21.

PATEL, A., BOERSMA, B.J. & PECNIK, R. 2016 The influence of near-wall density and viscosity gradients on turbulence in channel flows. *J. Fluid Mech.* **809**, 793–820.

PICKERING, E., RIGAS, G., SCHMIDT, O.T., SIPP, D. & COLONIUS, T. 2021 Optimal eddy viscosity for resolvent-based models of coherent structures in turbulent jets. *J. Fluid Mech.* **917**, A29.

PIROZZOLI, S. 2014 Revisiting the mixing-length hypothesis in the outer part of turbulent wall layers: mean flow and wall friction. *J. Fluid Mech.* **745**, 378–397.

PIROZZOLI, S. & BERNARDINI, M. 2011 Turbulence in supersonic boundary layers at moderate Reynolds number. *J. Fluid Mech.* **688**, 120–168.

PIROZZOLI, S. & BERNARDINI, M. 2013 Probing high-Reynolds-number effects in numerical boundary layers. *Phys. Fluids* **25** (2), 021704.

PIROZZOLI, S., BERNARDINI, M. & GRASSO, F. 2008 Characterization of coherent vortical structures in a supersonic turbulent boundary layer. *J. Fluid Mech.* **613**, 205–231.

PUJALS, G., GARCÍA-VILLALBA, M., COSSU, C. & DEPARDON, S. 2009 A note on optimal transient growth in turbulent channel flows. *Phys. Fluids* **21** (1), 015109.

REYNOLDS, W.C. & HUSSAIN, A.K.M.F. 1972 The mechanics of an organized wave in turbulent shear flow. Part 3. Theoretical models and comparisons with experiments. *J. Fluid Mech.* **54** (2), 263–288.

SCHMID, P.J. & HENNINGSON, D.S. 2001 *Stability and Transition in Shear Flows*. Springer.

SCHOPPA, W. & HUSSAIN, F. 2002 Coherent structure generation in near-wall turbulence. *J. Fluid Mech.* **453**, 57–108.

SMITH, C.R. & METZLER, S.P. 1983 The characteristics of low-speed streaks in the near-wall region of a turbulent boundary layer. *J. Fluid Mech.* **129**, 27–54.

SONG, Y., ZHANG, P., LIU, Y. & XIA, Z. 2022 Central mean temperature scaling in compressible turbulent channel flows with symmetric isothermal boundaries. *Phys. Rev. Fluids* **7** (4), 044606.

SONG, Y., ZHANG, P. & XIA, Z. 2023 Predicting mean profiles in compressible turbulent channel and pipe flows. *Phys. Rev. Fluids* **8** (3), 034604.

SPINA, E.F., SMITS, A.J. & ROBINSON, S.K. 1994 The physics of supersonic turbulent boundary layers. *Annu. Rev. Fluid Mech.* **26** (1), 287–319.

TAIRA, K., HEMATI, M.S., BRUNTON, S.L., SUN, Y., DURAISAMY, K., BAGHERI, S., DAWSON, S.T.M. & YEH, C.-A. 2020 Modal analysis of fluid flows: applications and outlook. *AIAA J.* **58** (3), 998–1022.

TOWNSEND, A.A.R. 1976 *The Structure of Turbulent Shear Flow*, 2nd edn. Cambridge University Press.

TREFETHEN, L.N. 2001 *Spectral Methods in Matlab*. SIAM.

TREFETHEN, L.N., TREFETHEN, A.E., REDDY, S.C. & DRISCOLL, T.A. 1993 Hydrodynamic stability without eigenvalues. *Science* **261** (5121), 578–584.

TRETTEL, A. & LARSSON, J. 2016 Mean velocity scaling for compressible wall turbulence with heat transfer. *Phys. Fluids* **28** (2), 026102.

VADAREVU, S.B., SYMON, S., ILLINGWORTH, S.J. & MARUSIC, I. 2019 Coherent structures in the linearized impulse response of turbulent channel flow. *J. Fluid Mech.* **863**, 1190–1203.

VOLPIANI, P.S., IYER, P.S., PIROZZOLI, S. & LARSSON, J. 2020 Data-driven compressibility transformation for turbulent wall layers. *Phys. Rev. Fluids* **5** (5), 052602.

WALZ, A. 1969 *Boundary Layers of Flow and Temperature*. MIT.

WILCOX, D.C. 2006 *Turbulence Modeling for CFD*, 3rd edn. DCW Industries.

WILLIAMS, O.J.H., SAHOO, D., BAUMGARTNER, M.L. & SMITS, A.J. 2018 Experiments on the structure and scaling of hypersonic turbulent boundary layers. *J. Fluid Mech.* **834**, 237–270.

YAO, J. & HUSSAIN, F. 2020 Turbulence statistics and coherent structures in compressible channel flow. *Phys. Rev. Fluids* **5** (8), 084603.

YU, M. & XU, C. 2022 Predictive models for near-wall velocity and temperature fluctuations in supersonic wall-bounded turbulence. *J. Fluid Mech.* **937**, A32.

ZARE, A., GEORGIOU, T.T. & JOVANOVIĆ, M.R. 2020 Stochastic dynamical modeling of turbulent flows. *Annu. Rev. Control Rob. Auton. Syst.* **3** (1), 195–219.

ZARE, A., JOVANOVIĆ, M.R. & GEORGIOU, T.T. 2017 Colour of turbulence. *J. Fluid Mech.* **812**, 636–680.

ZHANG, C., DUAN, L. & CHOUDHARI, M.M. 2018 Direct numerical simulation database for supersonic and hypersonic turbulent boundary layers. *AIAA J.* **56** (11), 4297–4311.

ZHANG, P.-J.-Y., WAN, Z.-H., LIU, N.-S., SUN, D.-J. & LU, X.-Y. 2022 Wall-cooling effects on pressure fluctuations in compressible turbulent boundary layers from subsonic to hypersonic regimes. *J. Fluid Mech.* **946**, A14.

ZHANG, Y.-S., BI, W.-T., HUSSAIN, F., LI, X.-L. & SHE, Z.-S. 2012 Mach-number-invariant mean-velocity profile of compressible turbulent boundary layers. *Phys. Rev. Lett.* **109** (5), 054502.

ZHANG, Y.-S., BI, W.-T., HUSSAIN, F. & SHE, Z.-S. 2014 A generalized Reynolds analogy for compressible wall-bounded turbulent flows. *J. Fluid Mech.* **739**, 392–420.

ZHOU, K., DOYLE, J.C. & GLOVER, K. 1996 *Robust and Optimal Control*. Prentice Hall.